

# DSS1 restrains BRCA2's engagement with dsDNA for homologous recombination, replication fork protection, and R-loop homeostasis

Received: 3 January 2024

Accepted: 9 August 2024

Published online: 17 August 2024

 Check for updates

Yuxin Huang<sup>1,9</sup>, Wenjing Li<sup>1,9</sup>, Tzeh Foo<sup>2</sup>, Jae-Hoon Ji<sup>1,3</sup>, Bo Wu<sup>1</sup>, Nozomi Tomimatsu<sup>4</sup>, Qingming Fang<sup>1,3</sup>, Boya Gao<sup>5</sup>, Melissa Long<sup>5</sup>, Jingfei Xu<sup>6</sup>, Rouf Maqbool<sup>1</sup>, Bipasha Mukherjee<sup>2</sup>, Tengyang Ni<sup>1</sup>, Salvador Alejo<sup>7</sup>, Yuan He<sup>6</sup>, Sandeep Burma<sup>1,4</sup>, Li Lan<sup>5,8</sup>, Bing Xia<sup>2</sup> & Weixing Zhao<sup>1,3</sup> ✉

DSS1, essential for BRCA2-RAD51 dependent homologous recombination (HR), associates with the helical domain (HD) and OB fold 1 (OB1) of the BRCA2 DSS1/DNA-binding domain (DBD) which is frequently targeted by cancer-associated pathogenic variants. Herein, we reveal robust ss/dsDNA binding abilities in HD-OB1 subdomains and find that DSS1 shuts down HD-OB1's DNA binding to enable ssDNA targeting of the BRCA2-RAD51 complex. We show that C-terminal helix mutations of DSS1, including the cancer-associated R57Q mutation, disrupt this DSS1 regulation and permit dsDNA binding of HD-OB1/BRCA2-DBD. Importantly, these DSS1 mutations impair BRCA2/RAD51 ssDNA loading and focus formation and cause decreased HR efficiency, destabilization of stalled forks and R-loop accumulation, and hypersensitize cells to DNA-damaging agents. We propose that DSS1 restrains the intrinsic dsDNA binding of BRCA2-DBD to ensure BRCA2/RAD51 targeting to ssDNA, thereby promoting optimal execution of HR, and potentially replication fork protection and R-loop suppression.

Mutations or defects in *BRCA2* (Breast Cancer gene 2) predispose the affected individuals to breast, ovarian, and other cancers<sup>1,2</sup>. *BRCA2* interacts with RAD51 through eight BRC repeats and a C-terminal region<sup>3-6</sup>, facilitating RAD51 loading on the resected ssDNA (i.e., RAD51-ssDNA presynaptic filament formation) for DNA double-strand break (DSB) repair by homologous recombination (HR)<sup>6,7</sup>. Moreover, *BRCA2* protects perturbed DNA replication

forks from nucleolytic degradation (replication fork protection, RFP) and prevents DNA-RNA hybrid or R-loop accumulation<sup>8-10</sup>. As a result, *BRCA2* deficient cells show genomic instability and are hypersensitive to genotoxic agents and replication stress<sup>5,6,11</sup>. However, the molecular mechanism(s) governing *BRCA2*'s targeting of nucleic acid substrates during these processes remains elusive.

<sup>1</sup>Department of Biochemistry and Structural Biology, University of Texas Health and Science Center, San Antonio, TX 78229, USA. <sup>2</sup>Department of Radiation Oncology, Rutgers Cancer Institute of New Jersey and Robert Wood Johnson Medical School, New Brunswick, NJ 08903, USA. <sup>3</sup>Greehey Children's Cancer Research Institute, University of Texas Health Science Center at San Antonio, San Antonio, TX 78229, USA. <sup>4</sup>Department of Neurosurgery, University of Texas Health Science Center at San Antonio, San Antonio, TX 78229, USA. <sup>5</sup>Department of Radiation Oncology, Massachusetts General Hospital, Harvard Medical School, Boston, MA 02129, USA. <sup>6</sup>Department of Molecular Biosciences, Northwestern University, Evanston, IL, USA. <sup>7</sup>Department of Obstetrics & Gynecology, University of Texas Health Science Center, San Antonio, TX 78229, USA. <sup>8</sup>Department of Molecular Genetics and Microbiology, School of Medicine, Duke University, Durham, NC 27710, USA. <sup>9</sup>These authors contributed equally: Yuxin Huang, Wenjing Li. ✉ e-mail: [zhaow2@uthscsa.edu](mailto:zhaow2@uthscsa.edu)

DSS1, a biomarker for various cancers<sup>12–14</sup>, forms a stable complex with BRCA2 via its DSS1/DNA-binding domain (DBD)<sup>15</sup>, which comprises a helical domain (HD) and three oligonucleotide binding (OB) folds named OB1, OB2, and OB3. The DBD-DSS1 crystal structure reveals that DSS1 tunnels through the HD, extensively interact with HD and OB1, crosses over the interface between OB1 and OB2, and then turns back to the junction of HD and OB1 to encircle HDOB1 in a shape of “ $\sigma$ ”, while OB2 and OB3 of BRCA2 DBD form a tandem repeat that binds ssDNA<sup>15</sup>. DSS1 resides nearly on the opposite side of the OB-fold groove for nucleotide binding, so it was suspected that DSS1 should not affect the overall DNA binding capability of BRCA2 DBD. Previous work has shown that DSS1 is required for BRCA2’s protein stabilization and nuclear localization and provides the sole RPA interface within the BRCA2-DSS1 complex to facilitate RPA-RAD51 exchange on ssDNA during HR<sup>6,16,17</sup>. Notably, pathogenic mutations are heavily enriched in the DBD region, especially HD and OB1 subdomains<sup>18–22</sup>, and mutations in DBD that abolish the interaction between BRCA2 and DSS1 or other unknown activities are defective in HR<sup>18–22</sup>, highlighting the importance of the DBD domains and the interaction with DSS1 for BRCA2’s roles in tumor suppression. However, it has also remained mysterious for almost two decades why the therapeutic PARP-inhibitor-resistant (PIR) mutant BRCA2 (hereafter referred to as BRCA2<sup>PIR</sup>), which deletes the whole DBD of BRCA2, or the BRC-RPA (replication protein A) fusion polypeptide, whereas the 70 kDa subunit of RPA is fused to single or several BRC repeats from BRCA2, can restore nearly wild-type levels of HR in the BRCA2 deficient cells<sup>23–25</sup>. As DSS1 depletion phenocopies a BRCA2 defect in cells in terms of HR and genome maintenance, much remains to be learned regarding how DSS1 controls BRCA2’s functions and how either BRCA2<sup>PIR</sup> or BRC-RPA70 fusion polypeptide works in promoting HR.

Of note, Dss1 in *U. maydis* only loosely associates with OB1 in the C-terminal DBD of Brh2, which lacks 77% HD and whole OB3, and both the amino-terminal primary DNA binding domain of Brh2 and DNA act together to evict Dss1 from its C-terminal interaction surface to reveal the full DNA and RAD51 binding potential of Brh2 for efficient HR<sup>11,26,27</sup>. In contrast, mammalian BRCA2 forms a stable complex with DSS1 only when they are co-expressed together, and DSS1 does not alter the ability of BRCA2 to bind RAD51<sup>7,15</sup>. The tower domain in OB2 has been suspected to bind dsDNA, and molecular dynamics simulation suggests that DSS1 allosterically regulates the conformation of the tower domain of BRCA2<sup>15,28</sup>, but it is not clear whether and how DSS1 controls the DNA binding of human BRCA2. Herein, we provide evidence that DSS1, through its C-terminal helix, enables two configurations of the BRCA2 DBD: when in a ‘closed’ status, shaped like a “ $\sigma$ ”, anchored by the intact C-terminal helix of the wild-type DSS1, the DNA binding capability of HD and OB1 (especially towards dsDNA) is blocked. This ensures specific recruitment of BRCA2 to ssDNA and facilitates the formation of the RAD51-ssDNA presynaptic filament, thus activating HR; conversely, when in a suspected ‘open’ configuration, resembling a “ $\nu$ ”, due to alterations in the DSS1 C-terminal helix, the dsDNA binding potential of HD-OB1 is unleashed. This inadvertently directs the BRCA2/RAD51 assembly to dsDNA, which reduces HR efficiency. Furthermore, we found that the suppression of the dsDNA binding ability of BRCA2 DBD by the DSS1 C-terminal helix is also required for the proper action of BRCA2 in protecting replication forks from degradation and preventing R-loop accumulation.

## Results

### Enhancement of BRCA2-mediated RAD51 loading on ssDNA by DSS1

We first ascertained whether DSS1 impacts the BRCA2-mediated RAD51 targeting activity (i.e., loading on ssDNA over dsDNA) in a well-established homologous DNA pairing assay using purified full-length BRCA2 and BRCA2-DSS1 (Supplementary Fig. 1a–d). The reaction was conducted without RPA presence to gauge the direct effects of BRCA2

and BRCA2-DSS1 on ssDNA targeting of RAD51. As expected, homologous pairing by RAD51 was suppressed when excessive non-homologous dsDNA was mixed with the ssDNA substrate due to the latter acting as a DNA trap to sequester RAD51 away from ssDNA (Supplementary Fig. 1e, f). This inhibitory effect of dsDNA was alleviated upon the addition of an increasing amount of BRCA2 (Supplementary Fig. 1e, f). Importantly, the BRCA2-DSS1 complex proved to be much more effective than BRCA2 in the restoration of homologous pairing efficiency (Supplementary Fig. 1e, f). In agreement with this, miBRCA2<sup>7,29,30</sup>, a BRCA2-derived polypeptide that harbors the BRC4 repeat, the DSS1/DNA-binding domain DBD, and the C-terminal domain that is encoded by exon 27 and which we have termed the CTB (C-terminal Recombinase Binding Domain) (Fig. 1a and Supplementary Fig. 1b), exhibited lower activity in the same assay compared to the miBRCA2-DSS1 complex (Supplementary Fig. 1g, h). We next applied a magnetic bead-based pulldown assay to directly monitor the loading of RAD51 onto ssDNA (see Fig. 1b for the schematic). The RAD51 loading on ssDNA became strongly inhibited when dsDNA was added as a RAD51 trap (Fig. 1c). Consistent with results from the homologous DNA pairing assay, miBRCA2-DSS1 was much more adept than miBRCA2 at restoring RAD51-ssDNA association. We therefore concluded that DSS1 enhances the ability of BRCA2 to load RAD51 specifically onto ssDNA.

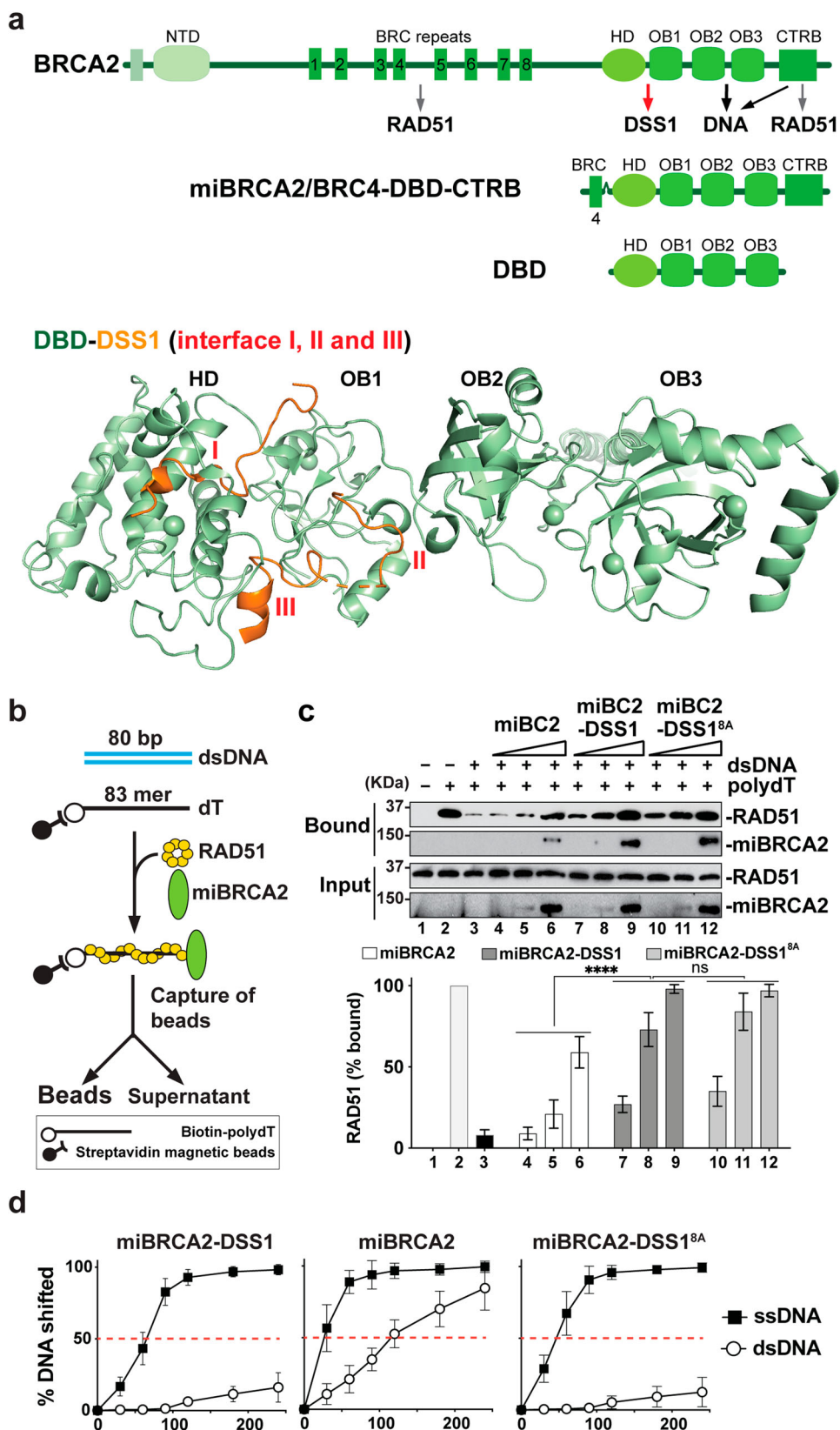
We previously described a DSS1 mutant with 8 amino acid residues in its solvent-exposed acidic loop<sup>15</sup> (Fig. 1a) mutated to alanine<sup>7</sup>. This DSS1<sup>8A</sup> mutant still stably associates with BRCA2 (Supplementary Fig. 1b), but the mutant BRCA2-DSS1<sup>8A</sup> complex becomes impaired in its ability to interact with RPA and in HR mediator activity<sup>7</sup>. Interestingly, in both the homologous DNA pairing and magnetic bead-based ssDNA targeting assays in the absence of RPA, we found that miBRCA2-DSS1<sup>8A</sup> exhibits a similar ability to target RAD51 on ssDNA for RAD51-ssDNA presynaptic filament formation as miBRCA2-DSS1 and is much more efficient than miBRCA2 in the same regard (Fig. 1b, c and Supplementary Fig. 1g, h)<sup>7</sup>. Notably, DSS1 alone does not promote RAD51 targeting on ssDNA, and the co-addition of separately purified DSS1 with miBRCA2 does not enhance the activity of the latter (Supplementary Fig. 1c, i, j). Based on the findings described above, we conclude that DSS1 enhances the ability of BRCA2 to target RAD51 to ssDNA. Importantly, DSS1-dependent ssDNA targeting of BRCA2-RAD51 requires complex formation between DSS1 and BRCA2, but the solvent-exposed acidic loop of DSS1, which mediates RPA interaction, appears to be dispensable in this regard.

### Negative regulation of BRCA2 dsDNA binding by DSS1

We note that DSS1 neither binds DNA nor interacts with RAD51<sup>7</sup>. Given this, we postulated that DSS1 acts by regulating an important functional attribute of BRCA2. We focused on how DSS1 affects the DNA binding properties of BRCA2 as it associates with a key region of the BRCA2 DBD. A DNA mobility shift assay was carried out to measure the DNA binding capacity of miBRCA2 and its complex with either DSS1 or DSS1<sup>8A</sup>. These experiments showed that miBRCA2 exhibits higher affinity for both ssDNA and dsDNA than either miBRCA2-DSS1 or miBRCA2-DSS1<sup>8A</sup> (Fig. 1d and Supplementary Fig. 1k). In particular, both miBRCA2-DSS1 and miBRCA2-DSS1<sup>8A</sup> demonstrated markedly diminished dsDNA binding compared to miBRCA2, while exhibiting a slight reduction ( $\leq 2$ -fold) in ssDNA binding (Fig. 1d and Supplementary Fig. 1k). Thus, DSS1 negatively regulates dsDNA binding by the BRCA2 DBD. Below, we furnish mechanistic insights into this dsDNA binding regulation role of DSS1 and its significance in the execution of HR and DSB repair in cells.

### DNA binding activity of HDOB1 and HDOB1-DSS1

We wished to test different subdomains within the BRCA2 DBD for dsDNA binding, as such an endeavor would set the stage for testing the regulatory function of DSS1 that we have discovered. For this purpose,



we expressed and purified the HD, OB1, HD-OB1 (HDOB1), and OB2-OB3 (OB23) domain(s) (Figs. 1a, 2a and Supplementary Fig. 2a, b) and examined their DNA binding properties in an electrophoretic mobility shift assay (EMSA) with either Cy5-labeled 80-mer ssDNA or 80-bp dsDNA as substrate. Consistent with results from previous studies<sup>15,31</sup>, OB23 binds ssDNA with an apparent  $K_d$  of 270 nM (Fig. 2a, b and

Supplementary Fig. 3a-e). We note that even though the OB2-appended tower domain has been speculated to bind dsDNA<sup>15</sup>, OB23 with an intact tower domain possesses little or no affinity for dsDNA (Fig. 2a, b and Supplementary Fig. 3a-e). Our analysis revealed that HDOB1 binds both ssDNA and dsDNA (Fig. 2a, b and Supplementary Figs. 3a, 4). Surprisingly, we found that HD alone binds ssDNA and also

**Fig. 1 | Facilitation of BRCA2-mediated RAD51 Targeting onto ssDNA over dsDNA by DSS1.** (See also Supplementary Fig. 1). **a** Schematic representation of BRCA2, miBRCA2, and DBD with various functional domains and interaction partners (top). Overall view of the mouse BRCA2-DBD (light green) in complex with DSS1 (orange; PDB: 1MIU) with three potential interfaces (I, II, and III, bottom). **b** Schematic representation of the magnetic bead-based pull-down assay to investigate RAD51 loading onto biotin-labeled ssDNA (dT83) in the presence of excessive dsDNA. **c** Western blot analyses to monitor RAD51 loading by miBRCA2 (lanes 4–6), miBRCA2-DSS1 (lanes 7–9), and miBRCA2-SS1<sup>8A</sup> (lanes 10–12) onto the ssDNA

substrate at 45 mM KCl condition. Bead without dT83 conjugation (lane 1) and pull-down without dsDNA (lane 2) served as controls. The mean values ( $\pm$ SD) from three independent experiments were correspondingly plotted at the bottom panel. ns not significant; \*\*\*\* $p \leq 0.0001$  (two-way ANOVA). **d** Quantification (mean  $\pm$  SD) of dsDNA and ssDNA binding by miBRCA2, miBRCA2-DSS1, and miBRCA2-DSS1<sup>8A</sup> from three independent experiments shown in Supplementary Fig. 1k at 90 mM KCl condition. miBRCA2 has significantly higher affinity to ssDNA and dsDNA than either miBRCA2-DSS1 or miBRCA2-DSS1<sup>8A</sup> with \*\*\*\* $P \leq 0.0001$  (two-way ANOVA). Source data are provided as a Source Data file.

dsDNA, with a preference for the former. In contrast, OBI displayed a lower affinity for either substrate under the same conditions but with a preference for dsDNA (Fig. 2a, b and Supplementary Fig. 3a–e). As anticipated from the X-ray crystallographic structure of mouse BRCA2 DBD in complex with DSS1<sup>15</sup>, we found no complex formation between DSS1 and OB23, but we could assemble a stable HDOB1-DSS1 complex for purification (Supplementary Fig. 2c). Importantly, testing of this HDOB1-DSS1 complex showed that it has little or no affinity for either ssDNA or dsDNA (Fig. 2c–e and Supplementary Fig. 4a–c). These results indicate that DSS1 prevents HDOB1 from binding DNA and provide evidence that maintenance of a “closed” HDOB1-DSS1 configuration (see below description) is required for DNA binding regulation.

### Role of the DSS1 C-terminal helix in HDOB1 regulation

The co-crystal structure of BRCA2 DBD-DSS1 reveals three interfaces that underpin DSS1-HDOB1 interactions<sup>15</sup> (Figs. 1a, 2a). In the interface where two entities are intricately interwoven, which we refer to as BRCA2-HDOB1/DSS1-N (I), the N terminal short helical segment (residues 8–13) of DSS1 tunnels through HD and is sandwiched within a hydrophobic pocket of HD, with the following five DSS1 residues (residues 14–18, all acidic) interacting with HD and OBI via salt bridges. The remaining two interaction interfaces occur between the C-terminal region of DSS1 (residues 39–63) and HDOB1 residues: one encompassing DSS1 residues 39–44 helps stabilize OBI-OB2 packing (II), while the other (i.e., the C-terminal helix, from residues 51–63) binds both HD and OBI domains and secures the OBI-HD interface (III)<sup>15</sup>. The three protein interaction interfaces lock DSS1 into a  $\sigma$ -like loop that encircles HDOB1, a DSS1 configuration that we refer to as the “closed” state (Figs. 1a, 2a, c). Consistently, the analysis, utilizing the newest AlphaFold2 for predicting potential conformations of the BRCA2-DBD-DSS1 complex<sup>32</sup>, indicates that DSS1 predominantly adopts a ‘closed’ conformation when complexed with BRCA2-DBD (Supplementary Fig. 5a). Of note, an ‘open’ conformational state is also plausible, characterized by varying degrees of DSS1 C-terminal helix displacement from the HDOB1 junction (Supplementary Fig. 5a). The AlphaFold prediction suggests that the interfaces I and II of DSS1 exhibit high pLDDT confidence scores, denoting strong predictive reliability, whereas the linker regions and the DSS1 C-terminal helix/interface III display increased conformational flexibility (Supplementary Fig. 5b).

We postulated that by embracing HDOB1, the two C-terminal interaction interfaces of DSS1 (II and III) either sterically restrict DNA accessibility to HDOB1 or attenuate DNA binding via negative allostery. To test this hypothesis, we designed a series of DSS1 mutants that delete different parts of its C-terminal region. These DSS1 mutants retain the ability to form a stable complex with HDOB1, and the various HDOB1-DSS1<sup>mut</sup> complexes (HDOB1-DSS1<sup>1–36</sup>, HDOB1-DSS1<sup>1–45</sup>, HDOB1-DSS1<sup>1–54</sup>, HDOB1-DSS1<sup>1–63</sup>) were purified from our *E. coli* expression system for testing in EMSA. In addition, a patient-derived mutation R57Q (c.170 G > A) within the C-terminal helix/interface (III) found in patients with different carcinomas (COSMIC)<sup>28</sup> was also tested within the context of the HDOB1-DSS1 complex. Importantly, our analyses revealed that the ability of DSS1 to dampen DNA binding by HDOB1 becomes progressively diminished in concordance with the extent of

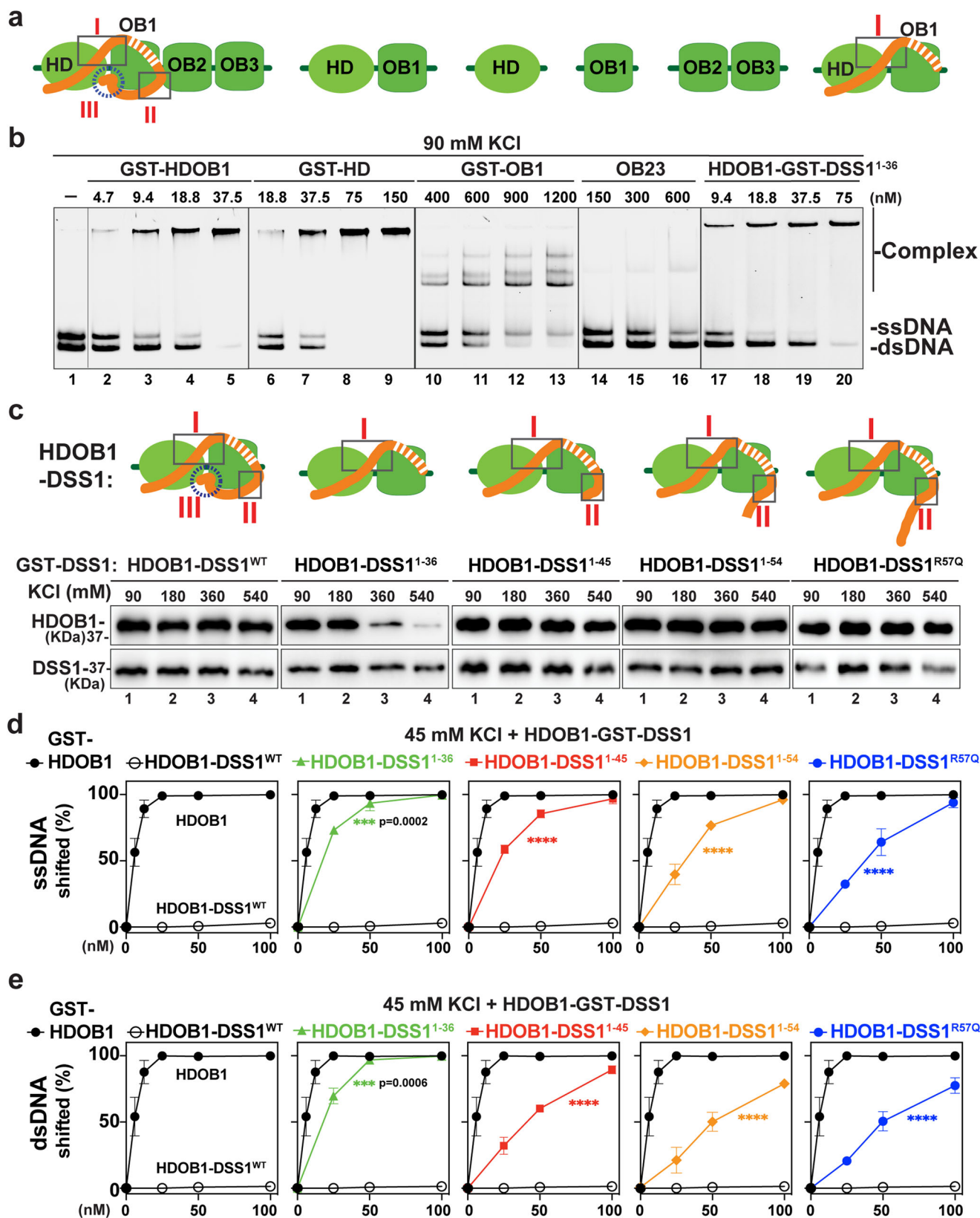
C-terminal truncation (Fig. 2c–e and Supplementary Figs. 2d, 4a–c). We also tested the salt sensitivity of the assembled HDOB1-DSS1 complexes and found that all but the DSS1<sup>1–36</sup> mutant (missing the C-terminal 34 residues that comprise interaction interfaces II and III) remain stably bound to HDOB1 even in the presence of 360 mM KCl (Fig. 2c). Thus, in support of our hypothesis, deletion of the DSS1 C-terminal helix motif/interface III and the cancer-associated R57Q mutation negate its ability to restrain DNA binding by HDOB1. Furthermore, we have noticed that increasing the KCl concentration in the EMSA leads to enhanced DNA binding by the HDOB1-DSS1 complexes, even though the higher salt concentration inhibits DNA binding by HDOB1, HD, or OB23 (Supplementary Figs. 6a, b, 7a, b). We surmised that a high salt concentration could mitigate the restrictive effect of DSS1 on DNA binding by HDOB1 via affecting the stability of the DSS1-HDOB1 interaction. Alternatively, or in addition, high salt could affect the conformation of HDOB1 and/or DSS1 in a manner that relaxes DNA binding restriction by DSS1. Accordingly, our data showed that both DBD and the less stable DBD-DSS1<sup>1–36</sup> complexes possess strong dsDNA and ssDNA binding capabilities (Supplementary Figs. 3a–e, 8a–e) and that elevated salt concentrations enhance the DNA binding propensity of DBD only when the DSS1 C-terminal helix is mutated (Supplementary Figs. 6a, b, 7a, b). As shown in Fig. 3a–d, DBD-DSS1<sup>1–54</sup> and DBD-DSS1<sup>R57Q</sup> displayed a markedly higher affinity for ssDNA and dsDNA binding compared to DBD-DSS1<sup>WT</sup>, particularly at 360 mM KCl (Fig. 3a–d). Collectively, our results provide evidence for the role of DSS1 in attenuating DNA binding by BRCA2 and that the DSS1 C-terminal helix is indispensable for the maintenance of the HDOB1-DSS1 “closed” state (Figs. 1a, 2a, 3a) to fulfill this DSS1 regulatory activity.

### Dependence of BRCA2-RAD51 targeting on the regulatory function of DSS1

We next investigated if the DSS1 mutations we constructed and examined above would impair the ssDNA targeting of BRCA2-RAD51. For this purpose, we co-expressed miBRCA2 with either DSS1<sup>1–54</sup> or DSS1<sup>R57Q</sup> in insect cells and then purified these complexes following the protocol established for the wild-type counterpart (Supplementary Fig. 2e). Importantly, when tested alongside miBRCA2-DSS1, both miBRCA2-DSS1<sup>1–54</sup> and miBRCA2-DSS1<sup>R57Q</sup> exhibited a markedly reduced capacity to facilitate RAD51 loading onto ssDNA (Fig. 3e, f). Despite this functional deficit in ssDNA targeting, both mutant miBRCA2-DSS1 complexes were just as adept as the wild-type complex in restoring homologous DNA pairing efficiency with RPA-coated ssDNA as a template (Supplementary Fig. 9a). Consistent with these results, we found that both mutant complexes are as proficient as their wild-type counterpart in RPA interaction (Supplementary Fig. 9b–d). Thus, DSS1 promotes the targeting of BRCA2-RAD51 to ssDNA, and this attribute is separable from the HR mediator activity of the BRCA2-DSS1 complex.

### Critical role of the DSS1 C-terminal helix in BRCA2 and RAD51 focus formation

In order to determine the physiological impact of DSS1-mediated ssDNA targeting of BRCA2-RAD51, we constructed HeLa-sh/siDSS1 cell



lines that ectopically express similar levels of shDSS1/siDSS1-resistant Flag-GFP-tagged DSS1 variants (DSS1<sup>WT</sup>res, DSS1<sup>1-54</sup>res, or DSS1<sup>R57Q</sup>res) or harbor the empty vector (Flag-GFP-vector), where the endogenous DSS1 could be eliminated by either a stably integrated, doxycycline-inducible shRNA or a siRNA against DSS1 (Supplementary Fig. 10a). Consistent with previous reports<sup>7,17</sup>, depletion of DSS1 led to

diminished BRCA2 nuclear localization, which was restored by the expression of DSS1<sup>WT</sup>res (Supplementary Fig. 10b, c). Notably, both DSS1<sup>1-54</sup>res and DSS1<sup>R57Q</sup>res were also able to support BRCA2 nuclear localization and chromatin association to a similar extent as the wild-type protein, in agreement with their capacity to form stable complexes with BRCA2 in vitro. We then examined the impact of the DSS1

**Fig. 2 | DSS1 modulates BRCA2-HDOBI DNA binding.** (See also Supplementary Figs. 2–7). **a** Schematic representation of DBD-DSS1 with three interfaces and various functional domains used in the study. **b** Representative gel of ssDNA (5 nM) and ssDNA (5 nM) binding by GST-HDOBI, GST-HD, GST-OBI, and OB23 and GST tagged DSS1<sup>1-36</sup>-HDOBI at 90 mM KCl condition from three independent experiments. **c** Schematic depicting HDOBI with wild-type or various mutants of DSS1 (top), and the complex stability was tested under increasing amounts of salt (KCl) in the GST bead pull-down experiments (bottom). Representative Western blot analyses to monitor His (6)-HDOBI and GST-DSS1 levels with anti-His or GST antibodies, respectively, from three independent experiments. **d** Quantification

(mean  $\pm$  SD) of ssDNA (5 nM) binding at 45 mM KCl condition by GST-HDOBI and GST tagged complexes (HDOBI-DSS1, HDOBI-DSS1<sup>1-36</sup>, HDOBI-DSS1<sup>1-45</sup>, HDOBI-DSS1<sup>1-54</sup>, and HDOBI-DSS1<sup>R57Q</sup>) from three independent experiments shown in Supplementary Fig. 4a, \*\*\*\* $p \leq 0.0001$  (two-way ANOVA). **e** Quantification (mean  $\pm$  SD) of dsDNA (5 nM) binding at 45 mM KCl condition by GST-HDOBI and GST tagged complexes (HDOBI-DSS1, HDOBI-DSS1<sup>1-36</sup>, HDOBI-DSS1<sup>1-45</sup>, HDOBI-DSS1<sup>1-54</sup>, and HDOBI-DSS1<sup>R57Q</sup>) from three independent experiments shown in Supplementary Fig. 4b, \* $p \leq 0.05$ ; \*\*\*\* $p \leq 0.0001$  (two-way ANOVA). Source data are provided as a Source Data file.

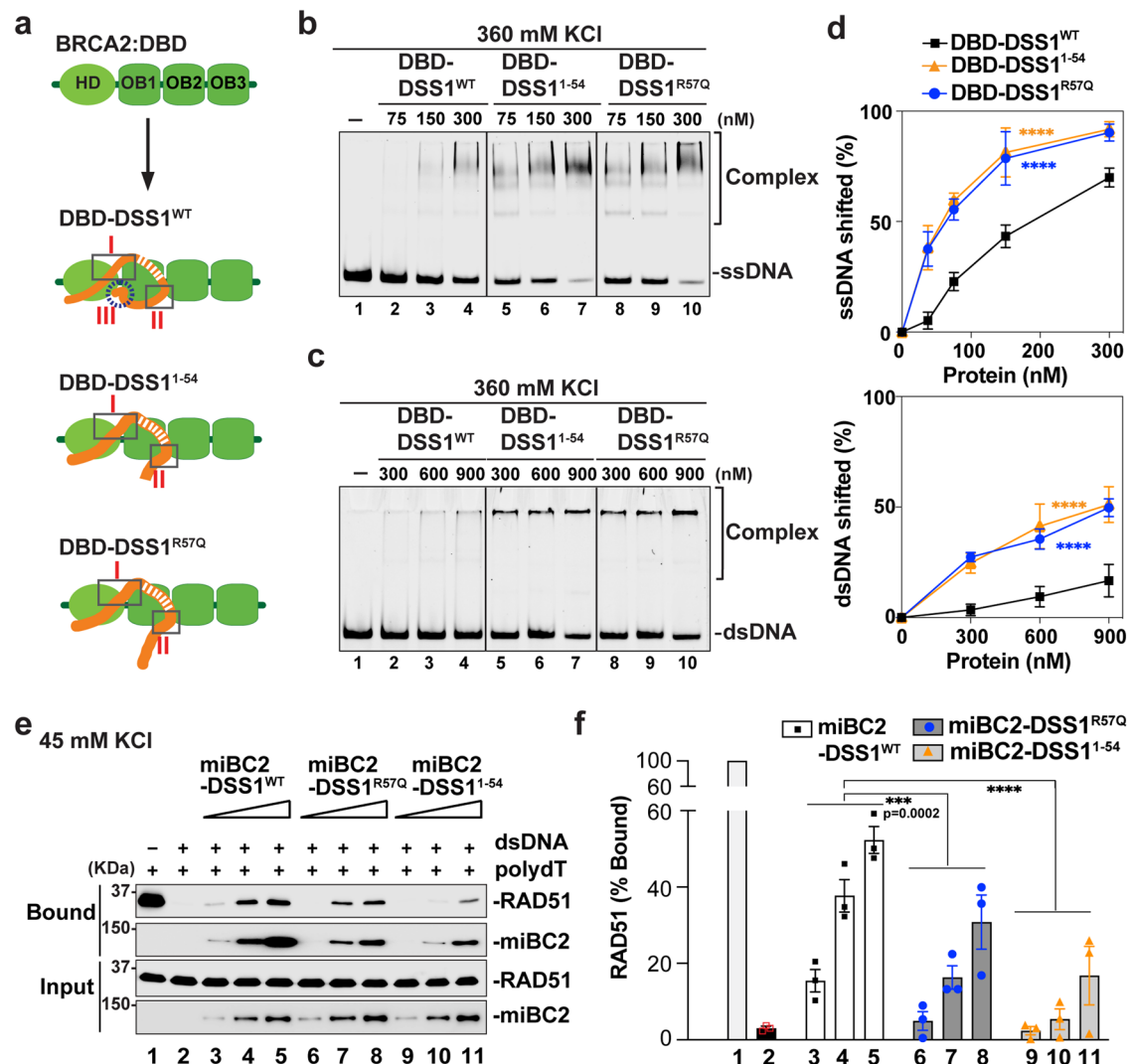


**Fig. 3 | Impact of DSS1 C-terminal Helix on DNA binding ability of DBD and targeting activity of miBRCA2-DSS1.** (See also Supplementary Figs. 8, 9). **a** Schematic representation of DBD-DSS1 complexes and their potential configurations. **b** Representative gel of ssDNA (5 nM) binding by DBD-DSS1<sup>WT</sup>, DBD-DSS1<sup>1-54</sup>, and DBD-DSS1<sup>R57Q</sup> at 360 mM KCl condition. **c** Representative gel of dsDNA (5 nM) binding by DBD-DSS1<sup>WT</sup>, DBD-DSS1<sup>1-54</sup>, and DBD-DSS1<sup>R57Q</sup> at 360 mM KCl condition. **d** Quantification (mean  $\pm$  SD) of ssDNA (top) and dsDNA (bottom) binding from at least three independent experiments shown in **b**, **c**, \*\*\*\* $p \leq 0.0001$  (two-way

ANOVA). **e** Western blot analyses to monitor RAD51 loading by miBRCA2-DSS1<sup>WT</sup> (lanes 3–5; 3.75 nM, 7.5 nM, and 15 nM), miBRCA2-DSS1<sup>R57Q</sup> (lanes 6–8; 3.75 nM, 7.5 nM, and 15 nM), and miBRCA2-DSS1<sup>1-54</sup> (lanes 9–11; 3.75 nM, 7.5 nM, and 15 nM) onto the ssDNA substrate at 45 mM KCl condition. Bead-biotin dT83 without dsDNA (lane 1) were served as a control. **f** Quantification of (e). The mean values ( $\pm$ SD) from three independent experiments were plotted, \*\*\* $p \leq 0.001$ , \*\*\*\* $p \leq 0.0001$  (two-way ANOVA). Source data are provided as a Source Data file.

mutations on BRCA2 foci formation in these cells before and after ionizing radiation (IR) exposure. As shown in Fig. 4a and Supplementary Fig. 10d, e, upon depletion of the endogenous DSS1, cells expressing DSS1<sup>WT</sup>res showed much more BRCA2-specific foci compared to those with the GFP-vector. Importantly, cells expressing either DSS1<sup>1-54</sup>res or DSS1<sup>R57Q</sup>res exhibited a pronounced deficiency in supporting BRCA2 focus formation at 4, 8, and 12 h following IR

exposure. The few BRCA2 foci seen in GFP-vector, DSS1<sup>1-54</sup>res or DSS1<sup>R57Q</sup>res expressing cells were also smaller in size compared with those in DSS1<sup>WT</sup>res cells (Fig. 4a). Furthermore, cells expressing GFP, DSS1<sup>1-54</sup>res or DSS1<sup>R57Q</sup>res also displayed a deficiency in the formation of BRCA2 foci without exogenous DNA damage (Fig. 4a and Supplementary Fig. 10d, e). In congruence with these results, RAD51 focus formation was also significantly impaired in cells that express either of

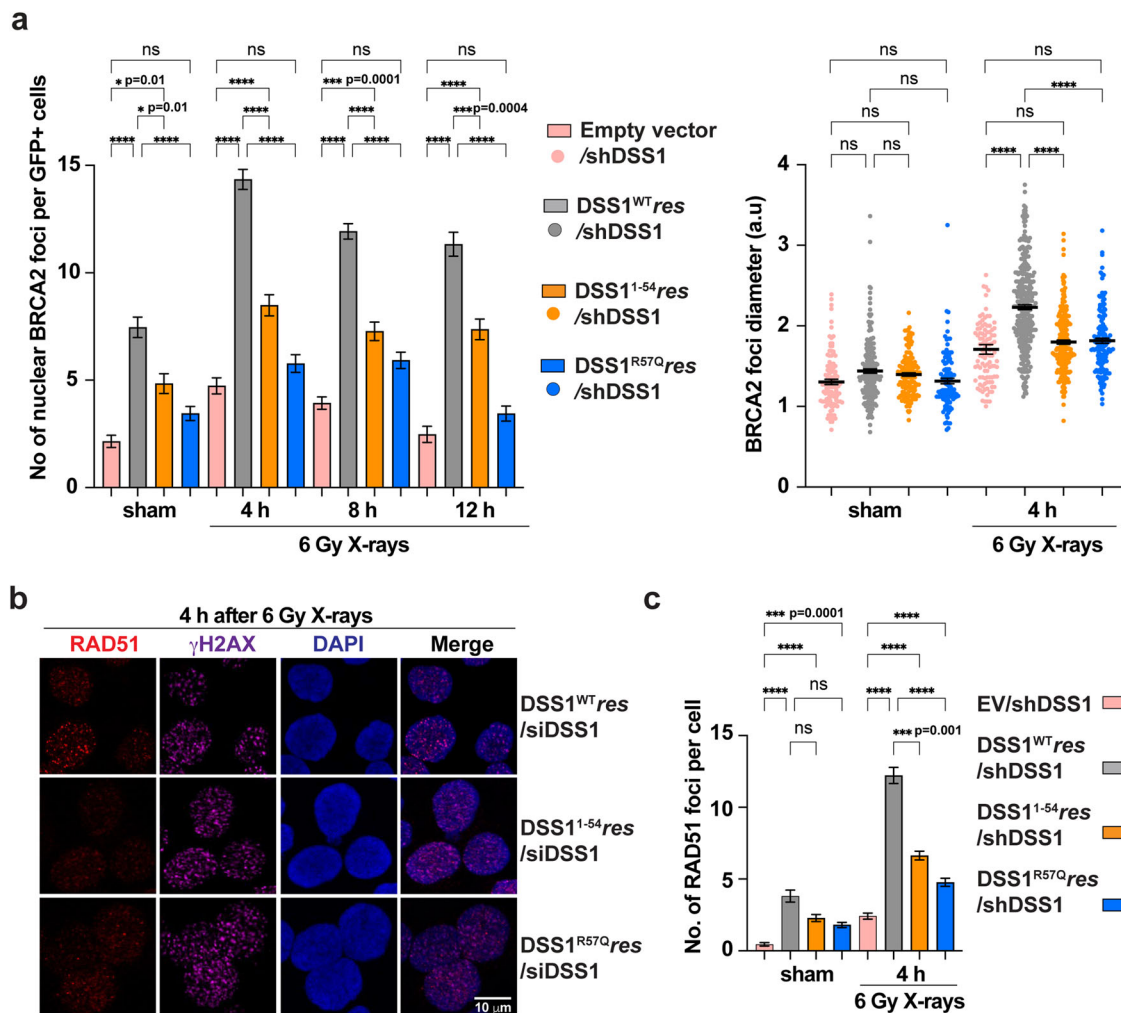


**Fig. 4 | Influence of DSS1 C-terminal Helix on BRCA2 and RAD51 Foci Formation.** (See also Supplementary Fig. 10). **a** Quantification of BRCA2 foci number per GFP-positive cell (left) and the foci diameter (right) at various time points after exposure to 6 Gy X-rays or sham irradiation. The mean values  $\pm$  SEM of at least three independent experiments is shown. ns not significant; \* $p \leq 0.05$ ; \*\*\* $p \leq 0.001$ ; and \*\*\*\* $p \leq 0.0001$  (ANOVA with the Kruskal–Wallis test). *P* values were calculated using two-way ANOVA for group comparison: Ev/shDSS1 vs DSS1<sup>WT</sup>/shDSS1, \*\*\*\* $p \leq 0.0001$ ; DSS1<sup>WT</sup>/shDSS1 vs DSS1<sup>1-54</sup>/shDSS1, \*\* $p \leq 0.01$ ; DSS1<sup>WT</sup>/shDSS1 vs DSS1<sup>R57Q</sup>/shDSS1, \*\*\*\* $p \leq 0.0001$ . **b** Representative micrographs of RAD51 foci (red) and  $\gamma$ H2AX (magenta) in HeLa cell nuclei at 4 h after exposure to 6 Gy X-rays.

Endogenous DSS1 was depleted by siRNA against DSS1. Blue: DAPI. **c** Quantification of RAD51 foci number per cell at 4 h after exposure to 6 Gy X-rays or sham irradiation. Endogenous DSS1 was depleted by doxycycline-induced shDSS1 expression. The mean values  $\pm$  SEM of at least three independent experiments is shown. ns not significant; \*\*\* $p < 0.001$ ; and \*\*\*\* $p \leq 0.0001$  (ANOVA with the Kruskal–Wallis test). *P* values were calculated using two-way ANOVA for group comparisons: Ev/shDSS1 vs DSS1<sup>WT</sup>/shDSS1, \*\*\*\* $p \leq 0.0001$ ; DSS1<sup>WT</sup>/shDSS1 vs DSS1<sup>1-54</sup>/shDSS1, \*\*\*\* $p \leq 0.0001$ ; DSS1<sup>WT</sup>/shDSS1 vs DSS1<sup>R57Q</sup>/shDSS1, \*\*\*\* $p \leq 0.0001$ . Source data are provided as a Source Data file.

the DSS1 mutants or harbor the empty vector when endogenous DSS1 was depleted (Fig. 4b, c and Supplementary Fig. 10f).

### Role of the DSS1 C-terminal helix in HR

We then utilized U2OS cells harboring the DR-GFP HR reporter<sup>33,34</sup> (Fig. 5a) to investigate the impact of the above mutations that compromise the functionality of the DSS1 C-terminal helix upon HR efficiency. In keeping with previous reports<sup>7,35,36</sup>, depletion of endogenous DSS1 by an siRNA severely compromised HR repair (Fig. 5b and Supplementary Fig. 11a, b). Ectopic overexpression of DSS1<sup>WT</sup>res in cells depleted of the endogenous DSS1 restored HR to near wild-type level, whereas expression of DSS1<sup>1-54</sup>res or DSS1<sup>R57Q</sup>res led to only partial complementation (Fig. 5b and Supplementary Fig. 11a, b). Next, we examined whether the two DSS1 mutations would render cells hypersensitive to agents that generate DNA lesions that require HR for repair, e.g., mitomycin C (MMC, a DNA crosslinking agent), olaparib (a poly (ADP-ribose) polymerase (PARP) inhibitor), and camptothecin (CPT, a topoisomerase I inhibitor). Clonogenic

survival tests of our HeLa-sh/siDSS1 cell lines revealed that cells expressing either GFP-DSS1<sup>1-54</sup>res or GFP-DSS1<sup>R57Q</sup>res were more sensitive to all three DNA-damaging agents (Fig. 5c, d and Supplementary Fig. 11c) compared to cells expressing GFP-DSS1<sup>WT</sup>res, while a similar cell-cycle profile was observed for all three cell lines (Supplementary Fig. 11d). Consistent with these results, levels of pRPA (S4/S8), a marker of ssDNA and unresolved DNA damage<sup>37</sup>, were significantly higher in GFP-DSS1<sup>1-54</sup>res or GFP-DSS1<sup>R57Q</sup>res expressing cells following either IR exposure or olaparib treatment (Fig. 5e).

### Role of the DSS1 C-terminal helix in replication fork protection

In addition to its pivotal role in DSB repair by HR, BRCA2 also plays a crucial role in safeguarding stalled replication forks against nucleolytic degradation under replication stress, where nascent DNA strands at stalled forks are susceptible to degradation by nucleases such as MRE11<sup>8,29,38</sup>. Notably, while DSS1, as a key partner to BRCA2, has been implicated in the process, its role in replication fork protection has not been directly examined using the DNA fiber assay. As such, we first

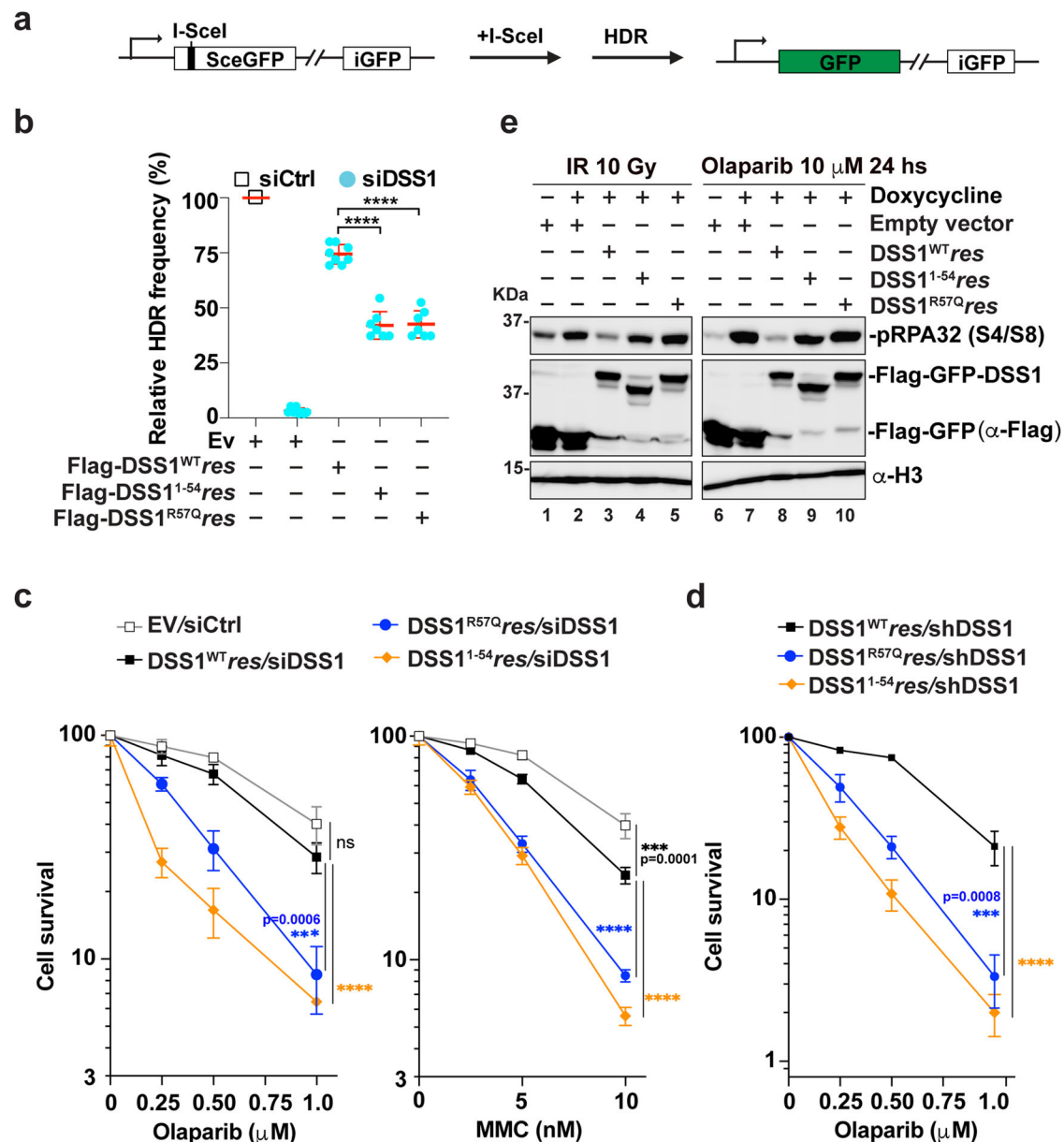


**Fig. 5 | Impact of DSS1 C-terminal Helix on HR Efficiency and Cell Survival.** (See also Supplementary Fig. 11). **a** Outline of the HR assay with the DR-GFP reporter in U2OS cells. **b** Quantification of results from HR assays in DR-U2OS cells with transient expression of empty vector, Flag-DSS1<sup>WT</sup>res, Flag-DSS1<sup>1-54</sup>res, or Flag-DSS1<sup>R57Q</sup>res after DSS1 knockdown and I-SceI expression. GFP-positive cells indicate the fraction of successfully completed HR events. The mean values ( $\pm$ SD) from 3–4 independent experiments were plotted, \*\*\*\* $p \leq 0.0001$ . **c**, **d** Survival curves of HeLa cells with stable expression of GFP-DSS1<sup>WT</sup>res, GFP-DSS1<sup>1-54</sup>res, or GFP-DSS1<sup>R57Q</sup>res after the treatment with increasing concentrations of Olaparib or MMC.

Endogenous DSS1 was depleted by doxycycline-induced shDSS1 expression or by siRNA against DSS1. The mean values ( $\pm$ SD) from three independent experiments were plotted, ns not significant; \*\* $p \leq 0.01$ ; \*\*\* $p \leq 0.001$ ; and \*\*\*\* $p \leq 0.0001$  (two-way ANOVA). **e** Representative Western blot from three independent experiments to show pRPA(S4/S8) levels at 6 h after exposure to 10 Gy X-rays or 10  $\mu$ M Olaparib 24 h treatment. Histone H3 serves as the loading control. Endogenous DSS1 was depleted by doxycycline-induced shDSS1 expression. Source data are provided as a Source Data file.

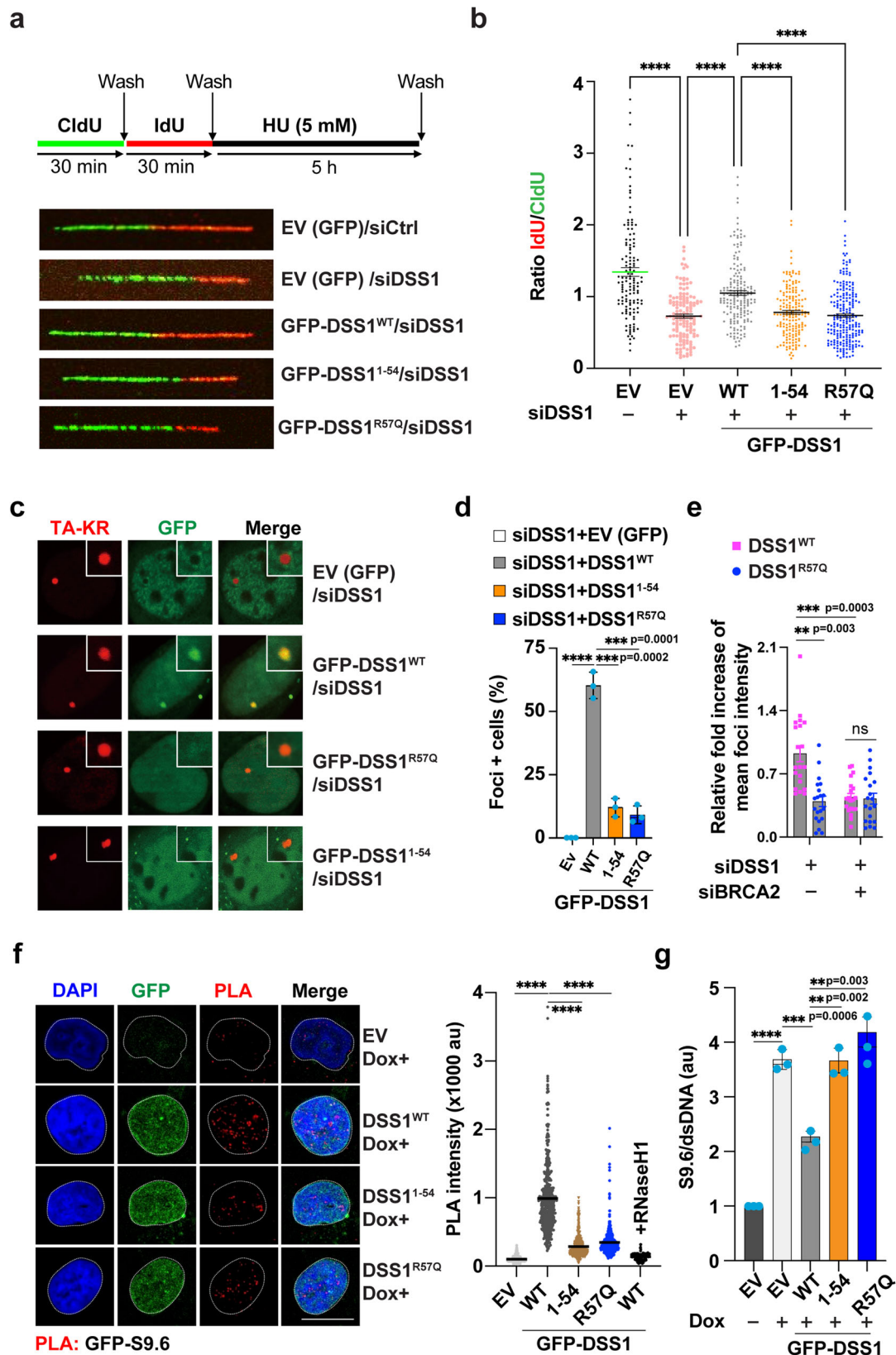
labeled DSS1-depletion HeLa cells with the thymidine analogs 5-Chloro-2'-deoxyuridine (CldU) followed by 5-Iodo-2'-deoxyuridine (IdU) before arresting DNA replication for 5 h with 5 mM HU (Fig. 6a) and then assessed potential fork degradation by determining the ratios of the lengths of IdU and CldU labeled replication tracts as previously described<sup>18,29,38</sup>. As shown in Fig. 6a, b and Supplementary Fig. 11e, DSS1-depleted cells showed a significantly reduced ratio of IdU/CldU tract length compared to control cells, consistent with the impact of BRCA2 knockdown, indicating nascent DNA degradation. Importantly, reduced ratios of IdU/CldU tract length were also seen in HeLa cells expressing the empty vector, GFP-DSS1<sup>1-54</sup>res or GFP-DSS1<sup>R57Q</sup>res, in

comparison with cells with GFP-DSS1<sup>WT</sup>res (Fig. 6b). This highlights the important role of the DSS1 C-terminal helix in replication fork preservation during replication stress.

#### Role of the DSS1 C-terminal helix in preventing R-loop accumulation

Excessive R-loops, three-stranded RNA-DNA hybrids that mostly arise during transcription or transcription-coupled processes, can compromise genome stability by causing conflicts during DNA replication. Specifically, head-on collision of the DNA replication machinery with R-loops can induce replication fork collapse, DNA breakage, and





chromosome rearrangements<sup>39,40</sup>. Importantly, BRCA2 and DSS1 are needed for either the avoidance of R-loop formation and/or the resolution of these potentially deleterious RNA-DNA hybrids<sup>9,41-43</sup>. To determine whether the DSS1 C-terminal helix is relevant for R-loop avoidance and/or resolution, we employed the DNA damage at RNA-transcribed sites (DART) system to interrogate in real-time the

recruitment of GFP-DSS1 (as an indicator of BRCA2-DSS1) at R-loop loci in live cells<sup>44,45</sup>. In the DART system, a tandem tetracycline-responsive element (TRE) array cassette with an adjacent reporter gene was stably integrated into the U2OS cell genome. KillerRed (KR), a light-activatable chromophore, is fused with either TetR (TetR-KR) or TetR with the transcription activator VP16 (TA-KR), to enable the generation of

**Fig. 6 | Requirement of DSS1 C-terminal Helix in Replication Fork Protection and R-loop Resolution.** (See also Supplementary Figs. 11, 12). **a** Schematic of replication fork stability assay with CldU and IdU labeling (top) and representative micrographs of fiber events in HeLa cells with stable expression of EV (GFP), GFP-DSS1<sup>WT</sup>res, GFP-DSS1<sup>I54</sup>res, or GFP-DSS1<sup>R57Q</sup>res (bottom). Endogenous DSS1 was depleted by siRNA against DSS1. **b** Dot plots of IdU to CldU tract length ratios for individual replication forks in HU-treated cells. The median value of 130–220 CldU and IdU tracts from three independent experiments. Data represent mean  $\pm$  SEM. Statistical analysis was performed using the two-sided student's *t*-test with \*\*\*\* $p < 0.0001$ . **c** U2OS-TRE cells transfected with pBROAD3 TA-KR and the expression vector of EV(GFP), GFP-DSS1<sup>WT</sup>, GFP-DSS1<sup>I54</sup>, or GFP-DSS1<sup>R57Q</sup> were light-activated and recovered 20 min before fixation. Representative images of GFP foci recruitment at sites of KR in each group were shown. **d** Foci-positive cells in each indicated group in Fig. 6c at sites of TA-KR were quantified ( $n = 30$ ). The mean values  $\pm$  SD of three independent experiments is shown, \*\*\*\* $p \leq 0.0001$  (two-sided student's *t*-test). **e** Fold increase of GFP-DSS1<sup>WT</sup> and GFP-DSS1<sup>R57Q</sup> foci intensity at

sites of TA-KR compared to background was quantified ( $n = 10$ , mean  $\pm$  SD) under the treatment of siDSS1 and siBRCA2. Statistical analysis was done with the two-sided student's *t*-test, ns not significant. **f** Representative micrographs of PLA foci (red) of DSS1 ( $\alpha$ -GFP) and R-loop (S9.6) in the nuclei of HeLa-shDSS1 cells stably expressing GFP-DSS1<sup>WT</sup>res, GFP-DSS1<sup>I54</sup>res or GFP-DSS1<sup>R57Q</sup>res after the treatment of CPT (10  $\mu$ M; 2 h) (left). Blue: DAPI. Green: GFP-DSS1. The foci formation was analyzed over 200 cells using ImageJ. Symbol: EV empty vector with GFP. au arbitrary unit. Scale bar: 10  $\mu$ m. Average values ( $\pm$ SEM) of PLA intensity for 500 nuclei from three independent experiments (right) were plotted. Statistical analysis was done with the two-sided student's *t*-test, \*\*\*\* $P \leq 0.0001$ . **g** Quantification (mean  $\pm$  SEM) of enrichment of R-loop (detected by S9.6 antibody) into genomic DNA of HeLa-shDSS1 cells stably expressing GFP-DSS1<sup>WT</sup>res, GFP-DSS1<sup>I54</sup>res, or GFP-DSS1<sup>R57Q</sup>res after the treatment of CPT (10  $\mu$ M; 2 h). au arbitrary unit. Statistical analysis was done from three independent experiments with the two-sided student's *t*-test, \*\*\*\* $p \leq 0.0001$ . Source data are provided as a Source Data file.

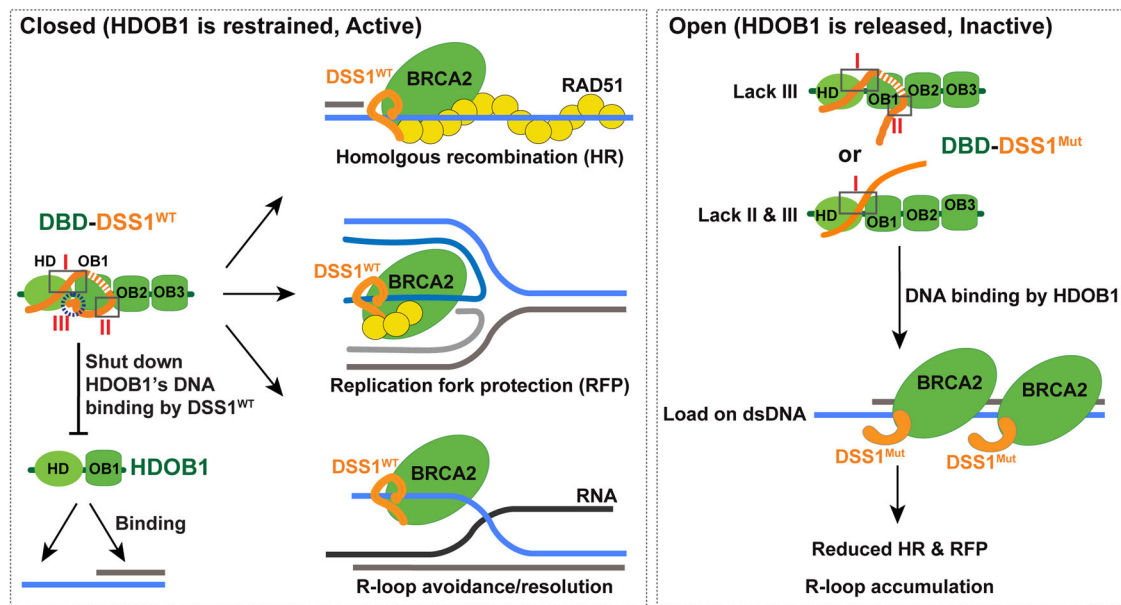


**Fig. 7 | Model for DSS1 in shutting down DNA binding ability of HDOB1 to promote BRCA2's functions.** In this model, DSS1, in an encircling arrangement around the HD and OB1 domains of BRCA2 DBD, locks the DBD-DSS1 complex in a closed conformation and shuts down the ds/ssDNA binding ability of HDOB1. Our work demonstrates that this conformation restrains the ability of BRCA2 DBD to engage with dsDNA, thereby facilitating BRCA2/RAD51 loading on ssDNA to

promote HR and RFP and also suppress the accumulation of R-loops. Conversely, mutations within the DSS1 C-terminal helix led to an open conformation of BRCA2-DSS1 and released its undesired dsDNA binding capability in BRCA2 DBD, consequently diminishing the effectiveness of BRCA2-DSS1 in promoting HR and RFP, and in R-loop suppression.

localized oxidative DNA damage and strand breaks at the TRE locus through the production of free radicals upon light activation. Both fusion proteins can bind to the TRE and target KR to the locus, but only TA-KR is able to locally activate reporter gene transcription. KR activation concurrent with ongoing transcription activated by TA-KR has been shown to induce robust R-loops at the TRE locus, while TA-Cherry, TetR-KR, or TetR-Cherry lead to few or no R-loops<sup>44,45</sup>. Using this system, we observed that GFP-DSS1 specifically colocalizes with TA-KR (Supplementary Fig. 12a) and that this recruitment is significantly diminished by the DSS1<sup>I54</sup> truncation mutation or the DSS1<sup>R57Q</sup> cancer-associated mutation (Fig. 6c, d and Supplementary Fig. 12b). Interestingly, BRCA2 depletion reduced the foci intensity of GFP-DSS1<sup>WT</sup>, but not GFP-DSS1<sup>R57Q</sup> (Fig. 6e and Supplementary Fig. 12c). Since either TetR-KR or TA-KR inflicts an equivalent amount of DNA damage, but TA-KR also induces R-loops at the locus, the findings above suggest that DSS1 is recruited to the R-loops incited by TA-KR and that efficient DSS1 colocalization with R-loops requires its intact C-terminal helix and its physical association with BRCA2. Furthermore, an in situ proximity ligation assay (PLA) was used to directly gauge the physical proximity of

DSS1 to R-loops detected by the S9.6 antibody. As illustrated in Fig. 6f and Supplementary Fig. 12d, cells harboring GFP-DSS1<sup>WT</sup>res exhibited more robust PLA signals than cells with empty vector, GFP-DSS1<sup>I54</sup>res or GFP-DSS1<sup>R57Q</sup>res, further underscoring the crucial role of the DSS1 C-terminal helix in the colocalization of BRCA2-DSS1 to R-loops. Importantly, we found that depletion of endogenous DSS1 by doxycycline treatment led to a remarkable increase in the level of R-loops (Fig. 6g and Supplementary Fig. 12e). Expression of GFP-DSS1<sup>WT</sup>res mitigated R-loop accrual significantly, while neither GFP-DSS1<sup>I54</sup>res nor GFP-DSS1<sup>R57Q</sup>res was effective in this regard (Fig. 6g). Taken together, our data suggest that the DSS1 C-terminal helix plays a pivotal role in recruiting BRCA2-DSS1 and averting R-loop accumulation.

## Discussion

Our study provides insights into the role of DSS1 in the modulation of BRCA2-mediated RAD51 presynaptic filament assembly on ssDNA versus dsDNA. Results, summarized in Fig. 7, underscore DSS1's pivotal role in tuning the conformation and DNA binding specificity of BRCA2 HDOB1, namely inhibiting its strong dsDNA binding activity and

enabling preferential loading of the BRCA2-DSS1 complex onto ssDNA. This regulation, in turn, enhances BRCA2-facilitated HR, RFP, and R-loop suppression.

### Novel DNA binding activities in HD and OB1 of BRCA2-DBD

OB2 and OB3 of BRCA2-DBD have long been established as a tandem repeat that binds to ssDNA, an understanding arrived at following the resolution of the DBD-DSS1-oligo(dT)<sub>9</sub> ternary complex structure two decades ago<sup>15</sup>. Yet, this short ssDNA oligo arguably provides limited DNA accessibility to other domains within DBD. Contrary to the common belief that the tower domain within OB2 binds dsDNA via the helix-turn-helix motif, our EMSA findings with purified OB2-OB3 do not corroborate this view. In a paradigm shift, we serendipitously found that both HD and OB1 possess a potent capacity for DNA binding, particularly dsDNA. Moreover, the accessibility of HDOB1 to dsDNA is fully blocked when it complexes with DSS1 in a closed configuration, resulting in a DBD-DSS1 complex that displays ssDNA binding specificity, akin to RPA.

Prior data sourced from cell-based HR reporter assays, family-based studies, and *in silico* prediction algorithms, including more recent high-performance random forest (RF) and naïve voting method (NVM), collectively delineate a preponderance of deleterious (functionally impaired) missense variants in the DBD, particularly HD and OB1 subdomains<sup>18–22</sup>. This underscores the pivotal roles of these domains in facilitating BRCA2's function in DNA repair through HR and its role in suppressing tumor development. It is noteworthy that several pathogenic variants within these domains arise from alterations of highly basic and aromatic residues that do not participate in DSS1 binding according to the crystal structure<sup>15</sup>. We speculate that these variants might affect the DNA binding of HDOB1, consequently influencing BRCA2's activity in one of two possibilities: (1) bypassing the DSS1 requirement like BRCA2<sup>PIR24,25</sup> or (2) alerting the dynamic conversion of BRCA2 DBD from engaging and disengaging with DNA<sup>46</sup> as detailed further below. Structural analyses to pinpoint residues directly interacting with dsDNA, coupled with additional biochemical and cellular investigations on the effects of these pathogenic mutations on BRCA2's functions in HR, RFP, and R-loop management, should shed significant light on this matter. Such studies will be of great need to help clarify the functional contributions of dsDNA binding by HDOB1 and its regulation by DSS1 for BRCA2 in these processes.

Interestingly, a recent report highlights the role of dsDNA-binding modules within BRCA2 in facilitating the interaction between the BRCA2-RAD51 complex and dsDNA, enabling dynamic sliding along dsDNA<sup>46</sup>. This diffusion-facilitated delivery mechanism subsequently triggers RAD51 nucleation on ssDNA emanating from the ds-ssDNA junction. In this context, our hypothesis is that the unique dsDNA binding ability inherent to HDOB1 discovered in this study could very likely contribute to the sliding dynamics of BRCA2, modulated further by DSS1 through conformational changes (as detailed in the ensuing discussion), during HR, resolution of R-loops, and safeguarding DNA replication fork integrity.

### Distinct regulatory functions of DSS1 in BRCA2-dependent genome maintenance

A substantial portion of our understanding regarding the regulatory influence of DSS1 on BRCA2 has emanated from investigations into the putative *U. maydis* counterpart, Brh2-Dss1<sup>11,26,27</sup>. Brh2's architecture is notably simpler, encompassing a distinct DNA binding domain at its N-terminus, a solitary BRC-like repeat in the middle, and a C-terminal DBD hosting just two OB folds and merely 30% of the HD when compared to its mammalian analog, BRCA2<sup>11,26,27</sup>. Notably, Brh2 also harbors an additional domain, referred to as CRE, situated at its extreme carboxyl terminus, which serves as a binding site for both RAD51 and Dss1<sup>11,26,27</sup>. In Brh2-Dss1, the N-terminus of Brh2 and DNA can displace

Dss1 from the complex, which presumably results from the absence of several key Dss1-binding residues in the HD domain of Brh2 compared with the HD domain of BRCA2. The subsequent release of Dss1 effectively unlocks Brh2's full potential in binding DNA and RAD51, thereby promoting HR<sup>11,26,27</sup>.

In recent years, further investigations into human BRCA2-DSS1 have unveiled substantial differences from the Brh2-Dss1 paradigm. In contrast to Brh2-Dss1, the BRCA2-DSS1 complex remains stable due to the intertwining of the polypeptide chains of BRCA2-HD with DSS1 (i.e., interaction interface I, Fig. 7). This intricately intertwined configuration necessitates co-expression and proper folding for complex formation<sup>7,15</sup>, which is also shown to suppress BRCA2 oligomerization<sup>47</sup>. Our previous work has established the indispensability of the stable BRCA2-DSS1 complex for its precise targeting of RPA-coated ssDNA. This targeting is facilitated by the physical interaction between DSS1 and RPA, with the complex effectively mimicking DNA to promote RPA-RAD51 exchange on ssDNA<sup>7</sup>. In this current study, we present evidence underscoring the requirement of its association with DSS1 for controlling BRCA2 DNA binding activity. DSS1's pivotal role lies in its ability to inhibit BRCA2's undesirable dsDNA binding activity of HDOB1 when in a closed configuration (Fig. 7, left). This inhibition promotes the loading of BRCA2/RAD51 onto ssDNA (i.e., focus formation) during HR and possibly also RFP (Fig. 7, left). Notably, any deletion or mutation in the C-terminal helix of DSS1 leads to an unraveling of DSS1's encircling structure, which we suspect results in an open configuration. However, we still lack direct experimental evidence, such as structural determination, to confirm this. This open configuration liberates a notable dsDNA binding capacity of BRCA2 DBD, but it concurrently impairs the ability of BRCA2 to promote HR, RFP, and cellular survival in the face of DNA damage (Fig. 7, right). Thus, we propose that DSS1's restricting BRCA2 to bind ssDNA only is essential for HR and possibly also RFP (Fig. 7, left) but note that further work is needed to confirm this model. Considering recent studies indicating the importance of BRCA2/RAD51 dsDNA binding activity for BRCA2's dynamic sliding along dsDNA<sup>46</sup> and their roles in RFP<sup>48,49</sup>, it is also plausible that the transition between open and closed configurations is dynamic and required for BRCA2-DSS1 to effectively engage and disengage with ds or ssDNA substrates during the different phases of HR reactions and replication fork maintenance. In this context, the C-terminal helix mutations in DSS1 may disrupt this dynamic conversion, thereby uncoupling the processes of engagement and disengagement from DNA. Consistent with this hypothesis, we observed that while the association of BRCA2 with chromatin remains unchanged, the focus formation of BRCA2 (presumably reflecting a concentrated presence on ssDNA) is diminished in cells expressing the C-terminal helix mutants of DSS1 (Fig. 4a and Supplementary Fig. 10c, d). Furthermore, our findings illustrate, for the first time, that the intact BRCA2-DSS1 complex is essential for their localization to R-loops, likely through its binding to the ssDNA region rather than the DNA/RNA hybrid portion of the R-loops (Supplementary Fig. 12f). Subsequent recruitment of RNase H2 and the augmentation of DDX5 activity could serve to resolve R-loops at these sites, as illustrated in recent reports<sup>9,41–43</sup>.

These mechanistic insights into human BRCA2-DSS1 help explain the activities of the aforementioned BRC-RPA fusion polypeptides and BRCA2<sup>PIR</sup> in facilitating RAD51-mediated HR: The fusion of BRC-RPA70 likely facilitates the delivery of RAD51 to ssDNA as it achieves coupling between the BRC element's RAD51 interaction ability and RPA's ssDNA binding specificity, mimicking the behavior of DBD-DSS1<sup>5,50</sup>. In the context of BRCA2<sup>PIR24,25</sup>, the undesired dsDNA binding by HDOB1 is eliminated through the deletion of DBD, allowing a bypass of the requirement of DSS1's encasing ability, while the loss of ssDNA binding activity could be compensated by PALB2 and/or BRCA1 within the BRCA2<sup>PIR</sup>-PALB2-BRCA1 complex, as evidenced from previous studies in hamster V-C8 and chicken DT40 cells<sup>30,51</sup>.

## Implications for cancer therapy

Given the pivotal role of the DSS1 C-terminal helix in orchestrating the functions of BRCA2 in HR, RFP, and R-loop avoidance/resolution, we propose that small molecule inhibitors or peptides that interfere with the interaction between the DSS1 C-terminal helix and the BRCA2 DBD, or ones that inhibit the specific encasing ability of DSS1, could serve as effective sensitizers for DNA-damaging therapies. These agents could potentially be integrated into existing radiotherapy or chemotherapy regimens, or used alongside PARP inhibitors to enhance the killing of tumor cells.

## Methods

### Plasmids construction

pDest8-MBP-His-BRCA2-Flag, pDest8-miBRCA2 (containing BRC repeat 4 (BRC4; residues 1496–1596), the DNA-binding domain (DBD; residues 2477–3194) and the C terminal RAD51-binding domain (CTRB; residues 3195–3418))-Flag, and pDest20-DSS1 were used for the expression of BRCA2-DSS1 and miBRCA2-DSS1 in insect cells as described<sup>7</sup>. Mouse Brca2 DBD (residues 2378–3115 aa) was introduced into MacroBac expression vector 438-c (Addgene 55220) to express DBD with an N terminal His-MBP tag (synthesized from GeneScript and codon optimized for insect cell expression). Human BRCA2 OB2 and OB3 (named OB23, 2808–3192 aa) was cloned into a pDEST20 vector to express OB23 with a N terminal GST tag. Human BRCA2 DBD subdomains, including HD (2479–2668 aa), OBI (2669–2807 aa), and HDOB1 (named HDOB1, 2479–2807 aa) were constructed in pGEX6P-1 vectors for protein expression in bacterial cells. Human BRCA2 HDOB1 was cloned into the pET28 vector to express HDOB1 with an N terminal His tag, and pGEX4T-DSS1 was used for the expression of GST-DSS1 as described<sup>7</sup>. DSS1-linker (CGAATTCCTCCGGGTCGA) + RBS-His<sub>6</sub>-HDOB1 synthesized from GeneScript was introduced into pGEX6P-1 vector to co-express GST-DSS1 and His-HDOB1 in bacterial cells. The mammalian Flag-GFP-DSS1 and Flag-DSS1 expression vectors pDest 3x Flag-pcDNA5-FRT/TO-DSS1res were generated from pEGFP-mouseDSS1 (a gift from Alan Ashworth). Quikchange site-directed mutagenesis was used to create the mutant forms of DSS1 (DSS1<sup>1–36</sup>, DSS1<sup>1–45</sup>, DSS1<sup>1–54</sup>, DSS1<sup>1–63</sup>, and DSS1<sup>R57Q</sup>) in the above expression vectors.

### Protein purification

**Purification of BRCA2-DSS1, miBRCA2-DSS1, DBD-DSS1, and OB23 from insect cells.** The bacmid production in *E. coli* strain DH10Bac, baculoviruses generation and amplification in SF9 cells, and protein expression in Hi5 cells (6 ml BRCA2/miBRCA2/DBD viruses and 6 ml DSS1 viruses per 300 ml culture) were done as described<sup>7,52</sup>. All purification steps were carried out at 0 to 4 °C. To prepare the extract, the frozen cell pellet (8 g, from 600 ml culture) was thawed and suspended in 50 ml of cell breakage buffer A (50 mM Tris-HCl, pH 7.5, 300 mM KCl, 1 mM EDTA, 0.01% Igepal-CA-630, 1 mM 2-mercaptoethanol ( $\beta$ -ME), 10% glycerol, 5 mM MgCl<sub>2</sub>, 2 mM ATP and the following protease inhibitors: aprotinin, chymostatin, leupeptin, and pepstatin A at 3  $\mu$ g/ml each, 1 mM PMSF, 1 mg/ml benzamidinium hydrochloride) for cell lysis using 10% strength sonication (Microtip, Branson Digital Sonifier) for 3 min (2 s pause on, 5 s pause off). After centrifugation (100,000 $\times$ g for 90 min), the clarified lysate was incubated with affinity resin for the following procedures.

For BRCA2-DSS1 and miBRCA2-DSS1, the clarified lysate from centrifugation (100,000 $\times$ g for 90 min) was incubated with 2 ml anti-Flag M2 affinity resin (Sigma) for 2 h. The beads were poured into a column (1.5  $\times$  15 cm) and washed with 25 ml buffer B (25 mM Tris-HCl, pH 7.5, 300 mM KCl 10% glycerol, 0.5 mM EDTA, 0.01% Igepal CA-630, and 1 mM DTT) for three times, before protein was eluted with 200  $\mu$ g/ml 3x-Flag peptide in buffer B three times (3 ml each). The Flag elutes of miBRCA2-DSS1 were pooled, concentrated, and loaded onto a Superdex200 Increase 10/300 GL column for further fractionation. The peak fractions were pooled, divided into 10  $\mu$ l portions, frozen in

liquid nitrogen, and stored at –80 °C. The DSS1 mutant forms of miBRCA2-DSS1 were expressed and purified using the same procedures.

For DBD-DSS1, the clarified lysate from centrifugation was incubated with 2 ml amylose resin for 2 h. After the resin was poured into a column (1.5  $\times$  15 cm) and washed with 100 ml buffer B, 50  $\mu$ g TEV enzyme in 10 ml buffer B was mixed with resin rocking overnight in a cold room, which will cleave the His-MBP-tag off MBP-DBD and GST tag off GST-DSS1. The flow-through fractions were collected, concentrated, and loaded onto a Superdex200 Increase 10/300 GL column for further fractionation. The peak fractions were pooled, divided into 10  $\mu$ l portions, frozen in liquid nitrogen, and stored at –80 °C. The DSS1 mutant forms of DBD-DSS1 were expressed and purified using the same procedures.

For OB2-OB3 (OB23), the clarified lysate from centrifugation was incubated with 2 ml Glutathione Sepharose 4 Fast Flow resin (GE Healthcare) for 1 h. The resin was washed with 25 ml buffer B for three times and then treated with 20 mM glutathione in buffer C (25 mM Tris-HCl, pH 8.0, 300 mM KCl) five times (2 ml each) to elute proteins. About 50  $\mu$ g TEV enzyme was added into the elute to cleave GST tag of GST-OB23, and the mixture was further fractionated in a 1 ml HiTrap Q HP Sepharose column (GE Healthcare) using a 20 ml gradient of 50–1000 mM KCl in buffer D (25 mM Tris-HCl, pH 7.5, 10% glycerol, 0.5 mM EDTA, 0.01% Igepal CA-630, and 1 mM DTT). The fractions containing OB2-OB3 were loaded onto a 1 ml Hitrap Heparin HP Sepharose column (GE Healthcare) and developed using a 12 ml gradient of 50–1000 mM KCl in buffer D.

**Purification of HD, OBI, HDOB1, and HDOB1-DSS1 from *E. coli* cells.** pGEX6P1-BRCA2-HD (2479–2668 aa), pGEX6P1-BRCA2 OBI (2669–2807 aa), pGEX6P1-BRCA2 HDOB1 (2479–2807 aa), and pGEX6P1-DSS1<sup>WT/1–63/1–54/1–45/1–36/R57Q</sup>-RBS-His<sub>6</sub>-HDOB1 were introduced into Rosetta (DE3) cells to express HD, OBI, HDOB1, and HDOB1-DSS1<sup>WT/1–63/1–54/1–45/1–36/R57Q</sup>, respectively. Single colonies were expanded in 25 ml LB medium overnight at 37 °C before dilution into 2 L fresh LB medium. Expression of GST-HD, GST-HDOB1, and His-HDOB1-GST-DSS1 were induced by the addition of 0.1 mM IPTG when the cell density had reached OD<sub>600</sub> = 0.8, and cells were harvested after an overnight (16–20 h) incubation at 16 °C. Expression of GST-OBI was induced by the addition of 1 mM IPTG when the cell density had reached OD<sub>600</sub> = 1.0, and cells were harvested after 4 h incubation at 37 °C. The pellet (10 g from 2 L culture) was suspended in 50 ml buffer A and lysate was prepared by sonication and centrifugation (100,000 $\times$ g for 30 min). All the purification steps were carried out at 0 to 4 °C.

For GST-HD and GST-HDOB1, the clarified lysate was incubated with 2 ml pre-equilibrated Glutathione Sepharose 4 Fast Flow resin (GE Healthcare) for 1 h. The resin was washed with 25 ml buffer B three times and then treated with 15 ml 20 mM Glutathione in buffer C to elute proteins (3 ml each five times). For GST-HDOB1, the Glutathione elutes were collected, concentrated, and loaded onto a Superdex200 Increase 10/300 GL column for further fractionation. For GST-HD, the Glutathione elutes were further fractionated in a 1 ml HiTrap SP HP Sepharose column (GE Healthcare) using a 20 ml gradient of 50–1000 mM KCl in buffer D, followed by a Superdex200 Increase 10/300 GL column. The peak fractions of both proteins were pooled, divided into 10  $\mu$ l portions, frozen in liquid nitrogen, and stored at –80 °C. For an untagged version of HD, 50  $\mu$ g of PreScission Protease was added into the Glutathione elutes to digest the GST tag off GST-HD overnight in a cold room, before being further processed with HiTrap SP HP Sepharose column and Superdex200 Increase 10/300 GL column.

For HDOB1-DSS1, the clarified lysate was incubated with 2 ml pre-equilibrated Glutathione Sepharose 4 Fast Flow resin (GE Healthcare) for 1 h. The resin was washed with 25 ml buffer B three times and then treated with 15 ml 20 mM glutathione in buffer C to elute proteins (3 ml each five times). Then the Glutathione elutes were pooled and

incubated with 2 ml Ni<sup>2+</sup>-NTA resin (GE Healthcare) for 30 min and washed with 20 ml buffer B. 12 ml of buffer B containing 250 mM imidazole was applied to elute the protein off resin (3 ml each for four times). The elutes were collected, concentrated, and loaded onto a Superdex200 Increase 10/300 GL column for further fractionation. The peak fractions were pooled, divided into 10  $\mu$ l portions, frozen in liquid nitrogen, and stored at  $-80^{\circ}\text{C}$ . The DSS1 mutant forms of HDOB1-DSS1 were purified using the same procedures.

For GST-OB1, the cell pellet was suspended in buffer A containing no salt for sonication. Inclusion bodies were collected by centrifugation (100,000 $\times$ g for 60 min), washed twice with 30 ml Wash buffer I (20 mM Tris-HCl pH 7.5, 500 mM NaCl, 2 M Urea, 2% Tween) and Wash buffer II (20 mM Tris-HCl pH 7.5, 500 mM NaCl, 2 M Urea) and solubilized in 10 ml dissolving buffer (20 mM Tris-HCl pH 7.5, 500 mM NaCl, 8 M Urea, 2 mM 2-mercaptoethanol) at room temperature for 30 min. After centrifugation (100,000 $\times$ g for 20 min), the clarified supernatant was dialyzed (8 h for each) against 2 L dialysis buffer I (20 mM Tris-HCl pH 7.5, 500 mM KCl, 3 M Urea, 1 mM DTT), 2 L dialysis buffer II (20 mM Tris-HCl pH 7.5, 500 mM KCl, 1 M Urea, 1 mM DTT) and 2 L dialysis buffer III (20 mM Tris-HCl pH 7.5, 500 mM KCl, 1 mM DTT) respectively, and the refolding was allowed to proceed during the dialysis (24 h) at  $4^{\circ}\text{C}$ . The solution containing the refolded protein was centrifuged for 30 min at 12,000 $\times$ g and incubated with 2 ml pre-equilibrated Glutathione Sepharose 4 Fast Flow resin for 1 h. The resin was washed with 25 ml buffer B three times and then treated with 15 ml 20 mM Glutathione in buffer C to elute proteins (3 ml each five times). The Glutathione elutes were collected, concentrated, and loaded onto a Superdex200 Increase 10/300 GL column for further fractionation. The peak fractions were pooled, divided into 10  $\mu$ l portions, frozen in liquid nitrogen, and stored at  $-80^{\circ}\text{C}$ .

**Other recombination proteins.** RAD51 and RPA were expressed in *E. coli* and purified to near homogeneity using previously described procedures<sup>53–55</sup>.

**DNA substrates and DNA binding assay.** Double-stranded DNA were assembled from oligonucleotide 1 (5'-Cy5-TTATCCTTTACTTTGA ATTCTATGTTAACTTTTACTTATTTGTATTAGCCGGACCTTATTT-CAATTATGTTTCAT-3') and oligonucleotide 2 (5'-ATGAACATAATTGA AATAAGGATCCGGCTAATACAAAATAAGTAAAAGGTTAAACATAGAA TTCAAAGTAAAGGATATAA-3'); DNA/RNA hybrid were assembled from oligonucleotide 3 (5'-IRDye<sup>®</sup> 800CW-ATCATCACCATAAC GTCGATGTATCAACTTCGATAGTACACCAATTA-3') and oligonucleotide 4 (5'-UUAUUGGUGACUUAUCGAAUUGAUACAUCG ACGUUAUGGUGAUGAU-3'). The asterisk indicates the oligonucleotide that was Cy5- or IRDye<sup>®</sup> 800CW labeled at its 5' ends in each substrate. These ssDNA, dsDNA or DNA/RNA hybrid substrates (5 nM each) were incubated with different domains of BRCA2-DBD, DBD-DSS1 or miBRCA2-DSS1 complexes at  $37^{\circ}\text{C}$  in 10  $\mu$ l buffer E (25 mM Tris-HCl, pH 7.5, 90 mM KCl unless indicated, 0.01% Igepal CA-630, 1 mM DTT, and 100  $\mu$ g/ml BSA) for 5 min. After the addition of 2  $\mu$ l 6 $\times$  gel loading buffer (60% glycerol, 120 mM Tris-HCl, pH 7.4, 3 mM EDTA, 0.025% orange G), the reaction mixtures were resolved by 10 or 4% native polyacrylamide gel electrophoresis in TAE buffer (40 mM Tris, 20 mM Acetate and 1 mM EDTA) at  $4^{\circ}\text{C}$ . The DNA species were visualized by the Cy5- or IRDye<sup>®</sup> 800CW- channel of the ChemiDoc MP Imaging System, and the data was quantified with the Image Lab software (Biorad).

**Homologous DNA pairing assay.** The reaction was assembled in buffer containing 25 mM Tris-HCl, pH 7.5, 2 mM MgCl<sub>2</sub>, 1 mM ATP, 100  $\mu$ g/ml BSA, and 65 mM KCl in a final volume of 12.5  $\mu$ l. All the steps were carried out at  $37^{\circ}\text{C}$ . In the standard reaction, 150-mer oligonucleotide ssDNA (5'-TCTTATTATGTCTCTTTTATTTTCATTTCTATATT

TATTCCTATTATGTTTTATTCATTTACTTATTCTTTATGTTTCATTTTT-TATATCCTTTACTTTATTTTCTCTGTTTATTCATTTACTTATTTTGTAT-TATCCTTATCTTATTTA-3'; 20 nM, 3  $\mu$ M nucleotides) was incubated with RAD51 (1  $\mu$ M) with or without indicated miBRCA2-DSS1 complex for 5 min, followed by the addition of <sup>32</sup>P-labeled or Cy5-labeled homologous dsDNA (5'-TAATACAAAATAAGTAAATGAATAAACAGAGAAAATAAAG-3', 5'-CTTTATTTTCTCTGTTTATTCATTTACTTATTTTG TAATA-3'; 10 nM, 0.4  $\mu$ M base pairs) and 4 mM spermidine hydrochloride. After 20 min of incubation, the reactions were mixed with an equal volume of 1% SDS containing 1 mg/ml proteinase K. Following a 10-min incubation at  $37^{\circ}\text{C}$ , the deproteinized reaction mixtures were resolved in 8% non-denaturing polyacrylamide gels in TAE buffer at  $4^{\circ}\text{C}$ . The gels were imaged and analyzed as above. For evaluating the targeting function of BRCA2, ssDNA (4 nM) was premixed with dsDNA (12 nM) before RAD51 (200 nM) was added to the reaction. For evaluating the targeting function of miBRCA2, ssDNA was premixed with dsDNA (60 nM) before RAD51 was added to the reaction. For experiments to check the recombination mediator function of miBRCA2, ssDNA (20 nM) was preincubated with RPA (150 nM) for 5 min before RAD51 (1  $\mu$ M) was added into the reaction.

**Targeting Assay via magnetic bead-based pulldown to assess RAD51 loading onto ssDNA.** Biotin-labeled 83 nucleotides polyT single-stranded DNA (dT<sub>83</sub>) was pre-conjugated to Streptavidin magnetic beads (Roche Applied Science) as described<sup>56–58</sup>. About 0.16  $\mu$ M RAD51 alone or RAD51 along with indicated miBRCA2-DSS1 complex was incubated with 2.5  $\mu$ l dT<sub>83</sub>-conjugated Strep beads (6 nM dT<sub>83</sub>) in buffer F (25 mM Tris pH 7.5, 45 mM KCl, 2 mM MgCl<sub>2</sub>, 0.01% Igepal CA-630, 1 mM ATP, 1 mM DTT, 100  $\mu$ g/ml BSA) in the presence of excessive double-stranded DNA (12 nM) as a trap for 5 min at  $37^{\circ}\text{C}$  (20  $\mu$ l reaction system). A 4  $\mu$ l aliquot of the reaction (20  $\mu$ l) was removed, combined with 4  $\mu$ l 2 $\times$  SDS-PAGE loading buffer, and set aside as the input fraction. The beads from the remaining portion of the reaction were captured by using a Magnetic Particle Separator (Roche Applied Science) and washed twice with 40  $\mu$ l of buffer G (25 mM Tris pH 7.5, 45 mM KCl, 1 mM ATP, 2 mM MgCl<sub>2</sub>, 0.05% Igepal CA-630) before treatment with 16  $\mu$ l 1 $\times$  SDS-PAGE loading buffer to elute proteins from the DNA. The input and eluate (5  $\mu$ l each) were analyzed by 12% SDS-PAGE and immunoblotting using antibodies ( $\alpha$ -RAD51 and  $\alpha$ -Flag) against RAD51 and miBRCA2 to determine their content of proteins.

**Affinity pulldown.** About 40 nM RPA was incubated with 200 nM of miBRCA2-DSS1<sup>WT</sup>, miBRCA2-DSS1<sup>I-54</sup>, and miBRCA2-DSS1<sup>R57Q</sup> on ice for 10 min in 35  $\mu$ l buffer H (25 mM Tris-HCl pH 7.5, 10% Glycerol, 150 mM KCl, 0.01% Igepal, 0.5 mM EDTA, 1 mM DTT) containing 0.05 mg/ml Benzonase Nuclease. About 5  $\mu$ l of the reaction mixtures was taken out as input, and the left mixtures were mixed with 15  $\mu$ l Glutathione Sepharose 4 Fast Flow resin at  $4^{\circ}\text{C}$  for another 40 min to capture protein complexes through the GST tag on DSS1. After washing the resin twice with 300  $\mu$ l buffer I (25 mM Tris-HCl pH 7.5, 10% Glycerol, 150 mM KCl, 0.05% Igepal, 0.5 mM EDTA, 1 mM DTT), bound proteins were eluted with 20  $\mu$ l 2% SDS at  $95^{\circ}\text{C}$  for 5 min. The inputs and SDS eluate, 8  $\mu$ l each, were analyzed by SDS-PAGE and immunoblotting using antibodies ( $\alpha$ -RPA70,  $\alpha$ -RPA32,  $\alpha$ -GST, and  $\alpha$ -Flag) against RPA, DSS1, and miBRCA2 to determine their content of proteins.

For protein complex stability of HDOB1-DSS1 and DBD-DSS1 via GST tag on DSS1, 200 nM wild-type or mutant forms of HDOB1-DSS1 or DBD-DSS1 were firstly incubated with 60  $\mu$ l Glutathione Sepharose 4 Fast Flow resin in binding buffer J (25 mM Tris-HCl pH 7.5, 1 mM DTT, 1 mM EDTA, 0.01% Igepal CA-630, and 90 mM KCl) supplemented with protease inhibitors for 30 min at  $4^{\circ}\text{C}$ . After being washed with 90  $\mu$ l buffer J twice to remove unbound protein complex, the resin was suspended in 125  $\mu$ l buffer J and aliquoted into four new Eppendorf

tubes (30  $\mu$ l/each). After the supernatant was removed after centrifugation, the resin in each tube was incubated for 5 min at 4 °C and washed with 30  $\mu$ l buffer J containing various concentrations of KCl (90, 180, 360, or 540 mM) three times. Bound proteins were eluted with 20  $\mu$ l 2xSDS loading buffer at 95 °C for 5 min, and 15  $\mu$ l of the samples was analyzed by SDS-PAGE. Coomassie blue staining was used for the experiments with DBD-DSS1 complexes, while immunoblotting using antibodies ( $\alpha$ -His and  $\alpha$ -GST) against HDOB1 and DSS1 was applied to determine the content of HDOB1-DSS1 complexes (see Immunoblot analysis section below for detailed antibody information).

**Mammalian cell culture and transfection.** HEK293T (ATCC), HeLa (ATCC), and U2OS clones (DR-GFP; a gift from Jeremy Stark) were grown in Dulbecco's modified Eagles medium (DMEM) supplemented with 10% fetal bovine serum (Sigma), 100  $\mu$ g/ml streptomycin, and 100 U/ml penicillin (Sigma). The cells were tested for mycoplasma contamination by Bionique testing labs (<http://www.bionique.com/>). Control siRNA (AllStars Neg. Control siRNA Cat. No.:1027281), DSS1 siRNA (5'-UAGAGGAUGACUUCUCUAAUC-3'), (BRCA2 siRNA (5'-UUGGAGGAAUAUCGUAGGUA-3'; 5'-GAAGAAUGCAGUUUAAUAdT dT-3') oligonucleotides were purchased from Qiagen. Dharmacon™ TRIPZ™ lentiviral shRNAs (RHS4696) against DSS1 were purchased from Horizon-PerkinElmer. Transfection of siRNA, mammalian expression vectors, shRNA, and pCMV-I-SceI-3xNLS was carried out using Lipofectamine 2000 (Invitrogen) according to the manufacturer's instructions. To create a FLP-in version of HeLa, we stably integrated a flippase recognition target (FRT) sequence into the cells by using the pFRT/lacZeo plasmid (Thermo Fisher Scientific). We tested Zeocin-resistant clones that had a single integration site detected by Southern blot for high-activity integration sites by using the mammalian  $\beta$ -galactosidase activity assay (Gal-Screen, Thermo Fisher Scientific). Clonal expansion of the selected colony established the HeLa-FRT cell line. To generate stable HeLa-FRT shDSS1 cells, TRIPZ™ lentiviral shRNAs against DSS1 were made from HEK293T cells by transfection with the pTRIPZ-shRNA plasmids, and individual HeLa clones were selected with 2  $\mu$ g/ml puromycin. To generate HeLa-FRT shDSS1 cell lines expressing Flag-GFP-DSS1 or their mutants, cells were transfected with their respective plasmids, and individual clones were selected with 200  $\mu$ g/ml hygromycin.

**Immunoblot analysis.** Protein was extracted from cells harvested 2 days after transfection with the indicated siRNAs or 3 days after 1  $\mu$ g/ml doxycycline treatment using NETN buffer (20 mM Tris-HCl pH 8, 420 mM NaCl, 1 mM EDTA, 0.5% Igepal-CA6300, 1 mM DTT, and Roche Protease Inhibitor Cocktail). Blots (20–50  $\mu$ g of total protein) were probed with the following antibodies: DSS1(SC28848, Santa Cruz; 1:500), BRCA2 (EMD Millipore, OP95-100UG; 1:1000), RAD51 (Novus Biologicals, NB100-148; 1:4000), Tubulin (2128 S, Cell Signaling; 1:2000), GAPDH (2118 S, Cell Signaling; 1:15,000), Lamin B1 (SC374015, Santa Cruz, 1:500), RPA70 (Abcam ab79398; 1:3000), p-RPA32 (S4/S8, A300-245A, Bethyl Laboratories; 1:2000), Phospho-Histone  $\gamma$ H2AX (9718 S, Cell Signaling; 1:2000), Flag M2-HRP (Sigma, A8592; 1:2000), GST-HRP (Invitrogen, MA4-004-HRP; 1:4000), His-HRP (Sigma, A7058, 1:3000), RPA32 (Abcam, ab2175; 1:2000), RPA70 (2267S, Cell Signaling; 1:2000) and Actin (Abcam, ab3280; 1:3000) according to the instructions provided by the manufacturers. If needed, the blots were incubated with HRP-conjugated secondary antibodies (Pierce 31450 for rabbit anti-mouse IgG-HRP; Sigma A6154 for goat anti-rabbit IgG-HRP; Santa Cruz Biotech SC2032 for goat anti-rat IgG-HRP) before visualization of protein signals using the ECL max kit (Biorad).

**DNA repair HR reporter assay.** The DR-U2OS cell line containing a single integrated copy of the DR-GFP reporter was used<sup>33,34</sup>. Exponentially growing cells were seeded in 6-well plates at  $2 \times 10^5$  cells per well prior to reverse transfection with 2  $\mu$ l siRNA (20  $\mu$ M) and 3  $\mu$ l

Lipofectamine™ RNAiMAX. Two days after siRNA transfection, cells were transfected with 1  $\mu$ g Flag-DSS1 and 0.75  $\mu$ g I-SceI expression vector (pCBASce) and 3  $\mu$ l Lipofectamine™ 2000. HR proficiency was determined by counting the fraction of GFP-positive cells using a BD FACS Calibur S at 72 h post-I-SceI transfection. The results were derived from 3 to 5 transfections of at least 3 independent experiments.

**Immunofluorescence microscopy and image analysis.** Cells were subjected to the treatment of 6 Gy X-rays (IR) followed by three washes with PBS, before being pre-extracted and fixed at different time points post-treatment. Pre-extraction was performed on ice for 10 min with cold cytoskeleton buffer (10 mM PIPES pH 6.8, 100 mM NaCl, 300 mM sucrose, 3 mM MgCl<sub>2</sub>, 1 mM EGTA, 0.5% Triton X-100) followed by 10 min with cytoskeleton stripping buffer (10 mM Tris-HCl pH 7.4, 10 mM NaCl, 3 mM MgCl<sub>2</sub>, 1% Tween 20 (v/v), 0.5% sodium deoxycholate). Next, cells were fixed with 4% paraformaldehyde on ice for 20 min, washed with PBS, and permeabilized for 10 min with 1% Triton X-100 in PBS. After being blocked in blocking buffer (0.2% Triton X, 5% Goat serum in PBS) on ice for 20 min, cells are incubated with primary antibodies in blocking buffer overnight at 4 °C in a humid chamber. The following primary antibodies were used RAD51(8875 S, Cell Signaling; 1:500),  $\gamma$ H2AX (05636, Millipore; 1:500), RPA (MABE285, Millipore, 1:500) and BRCA2 (Homemade from Xia Bing lab). Pre-extraction steps were omitted for the experiment with RAD51 and  $\gamma$ H2AX foci. Then, cells were washed in PBS three times, incubated with Alexa Fluor or FITC conjugated secondary antibodies (Jackson Immuno Research Laboratory) for 1 h at room temperature, and stained with DAPI for another 15 min, before slides were mounted using antifade mounting media (Cell signaling 9071). Images were captured using a Nikon Swept Field fluorescence microscope. The average number of RAD51 and RPA foci per nucleus and % cells with foci positive were determined after scoring at least 100 nuclei. Images were generated in the Core Optical Imaging Facility, which is supported by UTHSCSA, NIH-NCI P30 CA54174 (CTRC at UTHSCSA).

**Clonogenic survival assay.** HeLa cell lines stably expressing Flag-GFP-DSS1 wild-type or mutants were pretreated with doxycycline for 3 days or longer as described above. About 400 cells/well were seeded into 12-well plates, and treated with the indicated amount of MMC (Sigma), olaparib (Selleckchem) or camptothecin (Sigma) in regular growth medium for 11–12 days. Cells were fixed with methanol and stained with 0.5% crystal violet in methanol before colonies were counted. Clonogenic survival was determined for a given concentration of cells that were plated by dividing the number of colonies on each treated plate by the number of colonies on the untreated plate, taking the plating efficiency of untreated cells into account.

**Preparation of cytoplasmic and nuclear extracts.** The REAP method for the preparation of cytoplasmic and nuclear extracts was followed<sup>59</sup>. Briefly, HeLa cells from 10-cm dishes were washed with ice-cold phosphate buffer saline (PBS) pH 7.4, collected by centrifugation, resuspended in 900 ml of ice-cold PBS with 0.1% NP40 and protease inhibitors, and triturated five times using a p1000 micropipette. The lysed cell suspension was centrifuged for supernatant (this is the cytoplasmic fraction) and the pelleted nuclei was washed once with PBS with 0.1% NP40 and lysed by NETN buffer with protease inhibitors to yield the nuclear extract fraction. The cytoplasmic and nuclear fractions, 20  $\mu$ g each, were analyzed by immunoblotting for their content of BRCA2, Tubulin, and Lamin B1.

**Analysis of cell-cycle profiles.** For cell-cycle profile analysis,  $2 \times 10^6$  cells exponentially growing cells were washed with cold PBS, collected by centrifugation, and then fixed in 10 ml of ice-cold 70% ethanol/PBS for at least 2 days at 4 °C. The fixed cells were washed sequentially with

1 ml each of 30% ethanol/PBS and 0.05% BSA/PBS at 4 °C. Cells were incubated in the staining solution (40 µg/ml RNase A and 30 µg/ml propidium iodide in PBS) for 15 min at 37 °C in the dark. The stained cells were fractionated in a BD FACS Calibur S instrument and analyzed by the FlowJo software.

**DNA fiber assay.** DNA replication tracts were assessed by the single-molecule DNA fiber assay as described previously<sup>8,38</sup>. Briefly, exponentially growing cells were pulse-labeled with 100 µM CldU (30 min), washed three times in warm PBS, and exposed to 150 µM IdU (30 min) in a regular growth medium. Then cells were washed with warm PBS and incubated in a regular growth medium with 5 mM HU (Sigma-Aldrich). Labeled cells were collected by Trypsin digestion and resuspended in trypsin-EDTA buffer (Sigma-Aldrich, T3924) at  $1 \times 10^6$  cells per agarose plug. The preparation of agarose plugs, proteinase K treatment of plug, the plug washing,  $\beta$ -Agarase treatment of melted plug, DNA fiber combing, and immunodetection steps were performed exactly as described in the reference (STAR Protocols, 2022, 3:101371)<sup>60</sup> and the manufacturer's instructions of Genomic Vision ([www.genomicvision.com](http://www.genomicvision.com)). For immunodetection, Rat anti-BrdU (BU1/75 (ICRI), 1:20, Abcam, ab6326) and mouse anti-IdU (Clone B44, 1:5, BD Bioscience, 347580) antibodies were then applied in blocking solution to detect CldU and IdU, respectively. Secondary antibodies goat anti-rat 488 (Invitrogen, A11006) and donkey anti-mouse Cys3 (Invitrogen, A31570) were used at a dilution of 1:100. Replication tracts were imaged on the Olympus Fluoview FV3000 Confocal Laser Scanning Microscope System using a 63x oil objective. DNA tracts were measured using ImageJ v1.53 software and plotted in GraphPad Prism 10.

**DART assay with immunofluorescence staining.** U2OS-TRE cells were seeded in a 35 mm glass-bottom dish (MatTek, P35GC-1.5-14-C). For the DART assay, cells were exposed to a 15 W Sylvania cool white-fluorescent bulb for 20 min in a stage UVP (Upland, CA) for Killer-red (KR) activation. Cells were transfected with plasmids and siRNA 24 to 36 h before KR activation. Plasmids used in this study are GFP-empty vectors, GFP tagged DSS1<sup>WT</sup>, DSS1<sup>R57Q</sup>, or DSS1<sup>I-54</sup>. siRNAs used in this study are siControl (siCtrl), siBRCA2, and siDSS1. Transfection was done using Lipofectamine 2000 (Invitrogen) with a standard protocol. After KR activation, cells were recovered for 20 min at 37 °C before fixation. For fixation, cells were first rinsed with phosphate-buffered saline three times (PBS, BE17-516F) and fixed in 4% paraformaldehyde (PFA; Affymetrix, 19943 1 LT) for 15 min at room temperature. They were then washed with PBS on the rotating bed for 5 min and permeabilized using 0.1% Triton X-100 in PBS for 10 min, followed by another 5 min PBS wash on the rotating bed. Image acquisition was performed using the Olympus FV1000 confocal microscopy system (Cat. F10PRDMYR-1, Olympus). The frequency of the foci-positive cells was counted in thirty cells. Three independent experiments were done. The mean intensity was calculated by dividing the measured intensity of the selected area that colocalized with KR foci by ImageJ 1.52i software over the same size arbitrarily selected three areas in the nucleus ( $n = 10$ ).

**PLA (proximity ligation assay).** To analyze colocalization of DSS1/R-loop in HeLa-shDSS1 cells expressing wild-type or mutants Flag-GFP-DSS1, where endogenous DSS1 was depleted by doxycycline treatment (1 µg/ml, 72 h), proximity ligation assays (PLAs) were carried out as per manufacturers protocol (Duolink PLA kit; DUO92101; Sigma-Aldrich). Cells were cultured with glass-bottom dishes (SKU#801002; NEST) and pretreated with CPT (10 µM, 2 h) before removing doxycycline or DMSO (control). The cells were washed with PBS and permeabilized with 0.5% Triton X-100 in PBS, before being fixed with 1% of formaldehyde/PBS for 15 min. The fixed cells were washed twice with PBS and blocked with Duolink Blocking buffer for 1 h at 37 °C with humidity. Next, the cells were incubated with anti-GFP (Abcam, ab290)

and S9.6 (EMD Millipore, MABE1095) antibodies in Duolink antibody diluent at 4 °C overnight. In situ PLA probes (anti-mouse plus and anti-rabbit minus) were diluted 1:5 in Duolink antibody diluent and incubated to detect anti-GFP (rabbit) and anti-S9.6 (mouse) antibodies for 1 h at 37 °C. After being washed with 1x Wash buffer A solution three times for 5 min each, dishes were incubated at 37 °C for 30 min with 1x Duolink ligation buffer solution and then washed twice with 1x Wash buffer A solution for 5 min each. For amplification signals, 1x Amplification mix solution was prepared as per the manufacturer's instructions and added into dishes for incubation at 37 °C for 100 min in the dark. Lastly, dishes were washed with 1x Wash buffer B solution three times for 5 min each and 0.01x diluted Wash buffer B solution once for 5 min before being mounted with emulsion oil, including DAPI, and applied to the confocal microscope (FV3000; Olympus). Foci formation was analyzed using ImageJ (1.53a version; NIH) software.

**RNA/DNA hybrid slot blot.** To examine the R-loops levels in HeLa-shDSS1 cells expressing wild-type or mutants GFP-DSS1, where endogenous DSS1 was depleted by doxycycline treatment (1 µg/ml, 72 h), RNA/DNA hybrid slot blot assays were carried out as reported before<sup>61</sup>. After cells were treated with camptothecin (CPT; 10 µM, 2 h) and then further incubated for another 2 h, cells were directly lysed with DNazol (Invitrogen), and purified genomic DNA (gDNA) was sonicated (50% of power; 10/20 s interval of ON/OFF x3). The concentration of gDNA sheared was measured by Nanodrop. After being treated with RNase III (1 Unit; Invitrogen, AM2290) and RNase T1 (1000 Units; Thermo Fisher Sci., EN0541) at 37 °C for 15 min to cleave dsRNA and ssRNA, respectively, the indicated concentration of gDNA was applied to slot blot assay using Minifold I dot blot apparatus (Schleicher & Schuell). To remove the RNA/DNA hybrid, gDNA was treated with RNase H (10 Unit; NEB, M0297S) at 37 °C for 1 h. The membrane was blocked for 1 h at room temperature in 5% milk and incubated overnight with the S9.6 antibody (Millipore; MABE1095) at 1:1000 concentration. The membranes were developed using ECL detection reagents, and the signals were quantified using ImageJ software. Double-stranded DNA (dsDNA) antibody was used as a loading control.

### Statistical analysis

The statistical analysis was performed using Prism 10 (GraphPad Software, Inc., La Jolla, CA; <http://www.graphpad.com/quickcalcs/ttest1.cfm>) on the data from at least three independent experiments, as specified. Statistical significance was assessed by a two-tailed unpaired Student's *t*-test or two-way ANOVA. \* $P \leq 0.05$ , \*\* $P \leq 0.01$ , \*\*\* $P \leq 0.001$ , and \*\*\*\* $P \leq 0.0001$  were considered significant.

### Reporting summary

Further information on research design is available in the Nature Portfolio Reporting Summary linked to this article.

### Data availability

All data generated or analyzed during this study are included in this article and its Supplementary information files. Materials used in the analysis are available upon request from the corresponding author. Source data are provided with this paper in the Figshare Repository at <https://doi.org/10.6084/m9.figshare.25939660>.

### References

1. Wooster, R. et al. Identification of the breast cancer susceptibility gene BRCA2. *Nature* **378**, 789–792 (1995).
2. Gayther, S. A. et al. Variation of risks of breast and ovarian cancer associated with different germline mutations of the BRCA2 gene. *Nat. Genet.* **15**, 103–105 (1997).
3. Wong, A. K., Pero, R., Ormonde, P. A., Tavtigian, S. V. & Bartel, P. L. RAD51 interacts with the evolutionarily conserved BRC motifs in the

- human breast cancer susceptibility gene *brca2*. *J. Biol. Chem.* **272**, 31941–31944 (1997).
4. Esashi, F. et al. CDK-dependent phosphorylation of BRCA2 as a regulatory mechanism for recombinational repair. *Nature* **434**, 598–604 (2005).
  5. San Filippo, J., Sung, P. & Klein, H. Mechanism of eukaryotic homologous recombination. *Annu. Rev. Biochem.* **77**, 229–257 (2008).
  6. Zhao, W., Wiese, C., Kwon, Y., Hromas, R. & Sung, P. The BRCA tumor suppressor network in chromosome damage repair by homologous recombination. *Annu. Rev. Biochem.* **88**, 221–245 (2019).
  7. Zhao, W. et al. Promotion of BRCA2-dependent homologous recombination by DSS1 via RPA targeting and DNA mimicry. *Mol. Cell* **59**, 176–187 (2015).
  8. Schlacher, K. et al. Double-strand break repair-independent role for BRCA2 in blocking stalled replication fork degradation by MRE11. *Cell* **145**, 529–542 (2011).
  9. D'Alessandro, G. et al. BRCA2 controls DNA:RNA hybrid level at DSBs by mediating RNase H2 recruitment. *Nat. Commun.* **9**, 5376 (2018).
  10. Gomez-Gonzalez, B., Sessa, G., Carreira, A. & Aguilera, A. A new interaction between BRCA2 and DDX5 promotes the repair of DNA breaks at transcribed chromatin. *Mol. Cell Oncol.* **8**, 1910474 (2021).
  11. Holloman, W. K. Unraveling the mechanism of BRCA2 in homologous recombination. *Nat. Struct. Mol. Biol.* **18**, 748–754 (2011).
  12. Wei, S. J., Trempus, C. S., Cannon, R. E., Bortner, C. D. & Tennant, R. W. Identification of Dss1 as a 12-O-tetradecanoylphorbol-13-acetate-responsive gene expressed in keratinocyte progenitor cells, with possible involvement in early skin tumorigenesis. *J. Biol. Chem.* **278**, 1758–1768 (2003).
  13. Ma, Y. Y. et al. Identification of the deleted in split hand/split foot 1 protein as a novel biomarker for human cervical cancer. *Carcinogenesis* **34**, 68–78 (2013).
  14. Rezano, A. et al. Breast cancers with high DSS1 expression that potentially maintains BRCA2 stability have poor prognosis in the relapse-free survival. *BMC Cancer* **13**, 562 (2013).
  15. Yang, H. et al. BRCA2 function in DNA binding and recombination from a BRCA2-DSS1-ssDNA structure. *Science* **297**, 1837–1848 (2002).
  16. Li, J. et al. DSS1 is required for the stability of BRCA2. *Oncogene* **25**, 1186–1194 (2006).
  17. Jeyasekharan, A. D. et al. A cancer-associated BRCA2 mutation reveals masked nuclear export signals controlling localization. *Nat. Struct. Mol. Biol.* **20**, 1191–1198 (2013).
  18. Guidugli, L. et al. A classification model for BRCA2 DNA binding domain missense variants based on homology-directed repair activity. *Cancer Res.* **73**, 265–275 (2013).
  19. Guidugli, L. et al. Assessment of the clinical relevance of BRCA2 missense variants by functional and computational approaches. *Am. J. Hum. Genet.* **102**, 233–248 (2018).
  20. Hart, S. N. et al. Comprehensive annotation of BRCA1 and BRCA2 missense variants by functionally validated sequence-based computational prediction models. *Genet. Med.* **21**, 71–80 (2019).
  21. Richardson, M. E. et al. Strong functional data for pathogenicity or neutrality classify BRCA2 DNA-binding-domain variants of uncertain significance. *Am. J. Hum. Genet.* **108**, 458–468 (2021).
  22. Hu, C. et al. Classification of BRCA2 variants of uncertain significance (VUS) using an ACMG/AMP model incorporating a homology-directed repair (HDR) functional assay. *Clin. Cancer Res.* **28**, 3742–3751 (2022).
  23. Saeki, H. et al. Suppression of the DNA repair defects of BRCA2-deficient cells with heterologous protein fusions. *Proc. Natl Acad. Sci. USA* **103**, 8768–8773 (2006).
  24. Edwards, S. L. et al. Resistance to therapy caused by intragenic deletion in BRCA2. *Nature* **451**, 1111–1115 (2008).
  25. Sakai, W. et al. Secondary mutations as a mechanism of cisplatin resistance in BRCA2-mutated cancers. *Nature* **451**, 1116–1120 (2008).
  26. Zhou, Q., Mazloun, N., Mao, N., Kojic, M. & Holloman, W. K. Dss1 regulates interaction of Brh2 with DNA. *Biochemistry* **48**, 11929–11938 (2009).
  27. Zhou, Q. & Holloman, W. K. Dss1 regulates association of Brh2 with Rad51. *Biochemistry* **56**, 3318–3327 (2017).
  28. Alagar, S. & Bahadur, R. P. DSS1 allosterically regulates the conformation of the tower domain of BRCA2 that has dsDNA binding specificity for homologous recombination. *Int. J. Biol. Macromol.* **165**, 918–929 (2020).
  29. Kwon, Y. et al. DNA binding and RAD51 engagement by the BRCA2 C-terminus orchestrate DNA repair and replication fork preservation. *Nat. Commun.* **14**, 432 (2023).
  30. Siaud, N. et al. Plasticity of BRCA2 function in homologous recombination: genetic interactions of the PALB2 and DNA binding domains. *PLoS Genet.* **7**, e1002409 (2011).
  31. Rajagopalan, S., Andreeva, A., Rutherford, T. J. & Fersht, A. R. Mapping the physical and functional interactions between the tumor suppressors p53 and BRCA2. *Proc. Natl Acad. Sci. USA* **107**, 8587–8592 (2010).
  32. Jumper, J. et al. Highly accurate protein structure prediction with AlphaFold. *Nature* **596**, 583–589 (2021).
  33. Nakanishi, K. et al. Human Fanconi anemia monoubiquitination pathway promotes homologous DNA repair. *Proc. Natl Acad. Sci. USA* **102**, 1110–1115 (2005).
  34. Xia, B. et al. Control of BRCA2 cellular and clinical functions by a nuclear partner, PALB2. *Mol. Cell* **22**, 719–729 (2006).
  35. Kristensen, C. N., Bystol, K. M., Li, B., Serrano, L. & Brenneman, M. A. Depletion of DSS1 protein disables homologous recombinational repair in human cells. *Mutat. Res.* **694**, 60–64 (2010).
  36. Adamson, B., Smogorzewska, A., Sigoillot, F. D., King, R. W. & Elledge, S. J. A genome-wide homologous recombination screen identifies the RNA-binding protein RBMX as a component of the DNA-damage response. *Nat. Cell Biol.* **14**, 318–328 (2012).
  37. Mirman, Z., Cai, S. & de Lange, T. CST/Polalpha/primase-mediated fill-in synthesis at DSBs. *Cell Cycle* **22**, 379–389 (2023).
  38. Tagliatela, A. et al. Restoration of replication fork stability in BRCA1- and BRCA2-deficient cells by inactivation of SNF2-family fork remodelers. *Mol. Cell* **68**, 414–430.e418 (2017).
  39. Petermann, E., Lan, L. & Zou, L. Sources, resolution and physiological relevance of R-loops and RNA-DNA hybrids. *Nat. Rev. Mol. Cell Biol.* **23**, 521–540 (2022).
  40. Garcia-Muse, T. & Aguilera, A. R loops: from physiological to pathological roles. *Cell* **179**, 604–618 (2019).
  41. Bhatia, V. et al. BRCA2 prevents R-loop accumulation and associates with TREX-2 mRNA export factor PCID2. *Nature* **511**, 362–365 (2014).
  42. Sessa, G. et al. BRCA2 promotes DNA-RNA hybrid resolution by DDX5 helicase at DNA breaks to facilitate their repair double dagger. *EMBO J.* **40**, e106018 (2021).
  43. Wang, Y. et al. ZFP281-BRCA2 prevents R-loop accumulation during DNA replication. *Nat. Commun.* **13**, 3493 (2022).
  44. Yang, H. et al. FMRP promotes transcription-coupled homologous recombination via facilitating TET1-mediated m5C RNA modification demethylation. *Proc. Natl Acad. Sci. USA* **119**, e2116251119 (2022).
  45. Teng, Y. et al. ROS-induced R loops trigger a transcription-coupled but BRCA1/2-independent homologous recombination pathway through CSB. *Nat. Commun.* **9**, 4115 (2018).
  46. Belan, O. et al. Visualization of direct and diffusion-assisted RAD51 nucleation by full-length human BRCA2 protein. *Mol. Cell* **83**, 2925–2940.e2928 (2023).
  47. Le, H. P. et al. DSS1 and ssDNA regulate oligomerization of BRCA2. *Nucleic Acids Res.* **48**, 7818–7833 (2020).



48. Vugic, D. et al. Replication gap suppression depends on the double-strand DNA binding activity of BRCA2. *Nat. Commun.* **14**, 446 (2023).
  49. Halder, S. et al. Double-stranded DNA binding function of RAD51 in DNA protection and its regulation by BRCA2. *Mol. Cell* **82**, 3553–3565.e3555 (2022).
  50. Symington, L. S. & Gautier, J. Double-strand break end resection and repair pathway choice. *Annu. Rev. Genet.* **45**, 247–271 (2011).
  51. Al Abo, M. et al. Compensatory functions and interdependency of the DNA-binding domain of BRCA2 with the BRCA1-PALB2-BRCA2 complex. *Cancer Res.* **74**, 797–807 (2014).
  52. Zhao, W. et al. BRCA1-BARD1 promotes RAD51-mediated homologous DNA pairing. *Nature* **550**, 360–365 (2017).
  53. Ma, C. J., Gibb, B., Kwon, Y., Sung, P. & Greene, E. C. Protein dynamics of human RPA and RAD51 on ssDNA during assembly and disassembly of the RAD51 filament. *Nucleic Acids Res.* **45**, 749–761 (2017).
  54. Sigurdsson, S., Trujillo, K., Song, B., Stratton, S. & Sung, P. Basis for avid homologous DNA strand exchange by human Rad51 and RPA. *J. Biol. Chem.* **276**, 8798–8806 (2001).
  55. Xue, C. et al. Single-molecule visualization of human RECQ5 interactions with single-stranded DNA recombination intermediates. *Nucleic Acids Res.* **49**, 285–305 (2021).
  56. Chi, P., San Filippo, J., Sehorn, M. G., Petukhova, G. V. & Sung, P. Bipartite stimulatory action of the Hop2-Mnd1 complex on the Rad51 recombinase. *Genes Dev.* **21**, 1747–1757 (2007).
  57. Zhao, W. et al. Mechanistic insights into the role of Hop2-Mnd1 in meiotic homologous DNA pairing. *Nucleic Acids Res.* **42**, 906–917 (2014).
  58. Zhao, W. & Sung, P. Significance of ligand interactions involving Hop2-Mnd1 and the RAD51 and DMC1 recombinases in homologous DNA repair and XX ovarian dysgenesis. *Nucleic Acids Res.* **43**, 4055–4066 (2015).
  59. Nabbi, A. & Riabowol, K. Rapid isolation of nuclei from cells in vitro. *Cold Spring Harb. Protoc.* **2015**, 769–772 (2015).
  60. Moore, G., Jimenez Sainz, J. & Jensen, R. B. DNA fiber combing protocol using in-house reagents and coverslips to analyze replication fork dynamics in mammalian cells. *STAR Protoc.* **3**, 101371 (2022).
  61. Sollier, J. et al. Transcription-coupled nucleotide excision repair factors promote R-loop-induced genome instability. *Mol. Cell* **56**, 777–785 (2014).
- DMC awarded to W.Z. Additional funding was from NIH research grants including R01CA246807 (S.B.), R01CA282939 (L.L.), R01CA138804 (B.X.) and R01CA262227 (B.X.). S.B. is the Mays Family Foundation Distinguished Chair in Oncology.

### Author contributions

W.Z. conceived the study. W.Z., Y.H., W.L., S.B., L.L., and B.X. designed the experiments and analyzed the data. W.Z., Y.H., W.L., N.T., J.J., T.F., Q.F., B.G., M.L., B.M., B.W., T.N., R.M., and S.A. generated key materials or/and executed the experiments. J.X. and Y.H. perform the AlphaFold prediction. W.Z., Y.H., and W.L. wrote the original draft, and S.B., L.L., and B.X. reviewed and edited the paper with input from other authors.

### Competing interests

The authors declare no competing interests.

### Additional information

**Supplementary information** The online version contains supplementary material available at <https://doi.org/10.1038/s41467-024-51557-6>.

**Correspondence** and requests for materials should be addressed to Weixing Zhao.

**Peer review information** *Nature Communications* thanks Natsuko Chiba and the other, anonymous, reviewer(s) for their contribution to the peer review of this work. A peer review file is available.

**Reprints and permissions information** is available at <http://www.nature.com/reprints>

**Publisher's note** Springer Nature remains neutral with regard to jurisdictional claims in published maps and institutional affiliations.

**Open Access** This article is licensed under a Creative Commons Attribution-NonCommercial-NoDerivatives 4.0 International License, which permits any non-commercial use, sharing, distribution and reproduction in any medium or format, as long as you give appropriate credit to the original author(s) and the source, provide a link to the Creative Commons licence, and indicate if you modified the licensed material. You do not have permission under this licence to share adapted material derived from this article or parts of it. The images or other third party material in this article are included in the article's Creative Commons licence, unless indicated otherwise in a credit line to the material. If material is not included in the article's Creative Commons licence and your intended use is not permitted by statutory regulation or exceeds the permitted use, you will need to obtain permission directly from the copyright holder. To view a copy of this licence, visit <http://creativecommons.org/licenses/by-nc-nd/4.0/>.

© The Author(s) 2024

### Acknowledgements

We are grateful to Drs. Alan Ashworth and Daniel Durocher for reagents and technical advice, and Dr. William Gaines for a critical reading of the manuscript. This study was supported by a V Scholar Cancer Research Grant, a Young Investigator Award from Max and Minnie Tomerlin Voelcker Fund, the Cancer Prevention and Research Institute of Texas (RP210102), NIH research grants R01GM141091 and R01CA268641, and an American cancer society research scholar grant RSG-22-721675-01-